Texas A&M University
Mechanical Engineering Department
Turbomachinery Laboratory
Tribology Group

Computational Analysis of Gas Foil Bearings Integrating 1D and 2D Finite Element Models for Top Foil

Research Progress Report to the TAMU Turbomachinery Research Consortium

TRC-B&C-1-06

by

Luis San Andrés

Mast-Childs Professor

Principal Investigator

Tae Ho Kim

Research Assistant

June 2006

This material is based upon work supported by the National Science Foundation under Grant No. 0322925

Gas Foil Bearings for Oil-Free Rotating Machinery – Analysis Anchored to Experiments
NSF Funded Project, TEES # 32525/53900/ME

EXECUTIVE SUMMARY

Gas foil bearings (GFBs) are finding widespread usage in oil-free turbo expanders, APUs and micro gas turbines for distributed power due to their low drag friction and ability to tolerate high level vibrations, including transient rubs and severe misalignment, static and dynamic. The static load capacity and dynamic forced performance of GFBs depends largely on the material properties of the support elastic structure, i.e. a smooth foil on top of bump strip layers. Conventional models include only the bumps as an equivalent stiffness uniformly distributed around the bearing circumference. More complex models couple directly the elastic deformations of the top foil to the bump underlying structure as well as to the hydrodynamics of the gas film. This report details two FE models for the top foil supported on bump strips, one considers a 2D shell anisotropic structure and the other a 1D beam-like structure. The decomposition of the stiffness matrix representing the top foil and bump strips into upper and lower triangular parts is performed off-line and prior to computations coupling it to the gas film analysis governed by Reynolds equation. The procedure greatly enhances the computational efficiency of the numerical scheme.

Predictions of load capacity, attitude angle, and minimum film thickness versus journal speed are obtained for a GFB tested decades ago. 2D FE model predictions overestimate the minimum film thickness at the bearing centerline, but underestimate it at the bearing edges. Predictions from the 1D FE model compare best to the limited tests data; reproducing closely the experimental circumferential profile of minimum film thickness. The 1D top foil model is to be preferred due to its low computational cost. Predicted stiffness and damping coefficients versus excitation frequency show that the two FE top foil structural models result in slightly lower direct stiffness and damping coefficients than those from the simple elastic foundation model.

A three lobe GFB with mechanical preloads, introduced by inserting shims underneath the bump strips, is analyzed using the 1D FE structural model. Predictions show the mechanical preload enhances the load capacity of the gas foil bearing for operation at low loads and low shaft speeds. Energy dissipation, a measure of the bearing ability to ameliorate vibrations, is not affected by the preload induced. The mechanical preload has no effect on the static and dynamic forced performance of GFBs supporting large static loads.

TABLE OF CONTENTS

LIST OF TABLES

LIST OF FIGURES

NOMENCLATURE

$C_{\alpha\beta}$	Damping coefficients; $\alpha, \beta = X, Y$ [N·s/m]
c	Nominal radial clearance [m]
c_J	Measured journal radial travel [m]
c_m	Assembly radial clearance [m]
D	Top foil (bearing) diameter, $D = 2 \times R$ [m]
E	Top foil elastic modulus [Pa] or [N/ m^2]
e_X, e_Y	Journal eccentricity component [m], $e = \sqrt{e_X^2 + e_Y^2}$
F^e , F^G	FE element nodal force vector and global nodal force vector
f^1	Normal load vector for a four-node finite shell element.
h	Gas film thickness [m]
h_t	Shell thickness [m]
h_b	Bump height [m]
I	Moment of inertia [m^4]
i	Imaginary unit, $\sqrt{-1}$
j	Node number along circumferential direction
K^e , K^G	FE top foil element stiffness matrix and global nodal stiffness matrix
K^s	FE bump element stiffness matrix
K_f	Structural stiffness per unit area [N/m^3]
K'_f	Complex structural stiffness per unit area, $K'_f = K_f(1 + i\gamma)$ [N/m^3]
K_l	Structural stiffness per unit bump element [N/m]
$K_{\alpha\beta}$	Stiffness coefficients; $\alpha, \beta = X, Y$ [N/m]
k	Node number along the axial direction
k^{ij}	Stiffness matrices for a four-node finite element plate stiffness matrix
k_t	Shear correction coefficient (=5/6) in a shear deformable plate model [-]
L	Bearing axial width [m]
l_x	Pad circumferential length, $R(\Theta_t - \Theta_l)$ [m]
l_0	Half bump length [m]
l_{ex}	FE thin foil length in the circumferential direction [m]
l_{ey}	FE thin foil length in the axial direction [m]
M_{MN}	Bending moment per unit element length in a thin shell [N]
$m^{1,2}$	bending moment vectors for a four-node finite shell element
N_{MN}	Membrane or in-plane force per unit element length in a thin shell [N/m]
N_b	Number of bumps [-]
p	Hydrodynamic pressure in gas film [Pa]
p_a	Ambient pressure [Pa]
p_A	Average pressure along axial direction [Pa]
Q_m	Shear force per unit element length in a thin shell [N/m]
$Q^e_{1,2}$	Shear forces at the boundary of a FE element
$Q^e_{3,4}$	Bending moments at the boundary of a FE element

q	Transversely distributed load [N/m^2].
r_P	Preload on bearing [m]
R	Top foil (bearing) radius [m]
S_{fa} , S_{fc}	Stiffening factors for elastic modulus in the axial and circumferential directions [-]
s_0	Bump pitch [m]
t	Time [s]
t_b	Bump foil thickness [m]
t_t	Top (thin) foil thickness [m]
U^e , U^G	FE nodal displacement vector and global nodal displacement vector
u	Shell circumferential displacement (x direction)
u^e	FE nodal displacement
w	top foil transverse deflection [m]
X, Y	Coordinate system for the inertial axes [m]
x, z	Coordinate system on plane of bearing [m]
ϕ_x , ϕ_y	Shell rotation angles about the y and x axes
Φ	Journal attitude angle, $\tan^{-1}(e_x/e_y)$ [rad]
γ	Structural damping loss factor [-]
μ	Gas viscosity [Pa-s]
ν	Shell axial displacement (y direction)
$\nu_{1,2}$	Weight function for FE formulae
ν_p	Poisson's ratio [-]
ψ^e	Hermite cubic interpolation function
Θ	Top foil angular coordinate [rad]
Θ_p	Preload offset position [rad]
Ω	Rotor angular velocity [rad]
$\Omega_{threshold}$	Threshold speed of instability [Hz]
ω	Whirl frequency [rad]
$\omega_{threshold}$	Whirl frequency of unstable motions[Hz]
ω_n	Natural frequency of system [Hz]
WFR	$\omega_{threshold} / \Omega_{threshold}$ .Whirl frequency ratio [-]

Subscripts

$\alpha, \beta = X, Y$	Directions of perturbation for first order pressure fields
$M, N = x, y$	Directions of shell membrane and moment force

Superscripts

i,j =1-3	Row and column numbers for a four-node finite element plate stiffness matrix

I. INTRODUCTION

Implementing gas foil bearings (GFBs) in micro turbomachinery reduces system complexity and maintenance costs, and increases efficiency and operating life [1, 2]. Since the 1960s, tension tape GFBs and multiple leaf GFBs with and without backing springs, as well as corrugated bump GFBs, have been implemented as low friction supports in oil-free (small size) rotating machinery. In comparison to rolling element bearings and for operation at high surface speeds, both leaf GFBs and bump GFBs have demonstrated superior reliability in Air Cycle Machines (ACMs) of aircraft environmental control systems [3-6], for example. Figure 1 shows the configurations of two GFBs. In multiple overleaf GFBs, the compliance to bending from staggered structural foils and the dry-friction at the contact lines define their operational characteristics [5]. In corrugated bump GFBs, bump-strip layers supporting a top foil render a tunable bearing stiffness with nonlinear elastic deformation characteristics. In this type of bearing, dry-friction effects arising between the bumps and top foil and the bumps and the bearing inner surface provide the energy dissipation or damping characteristics [6].

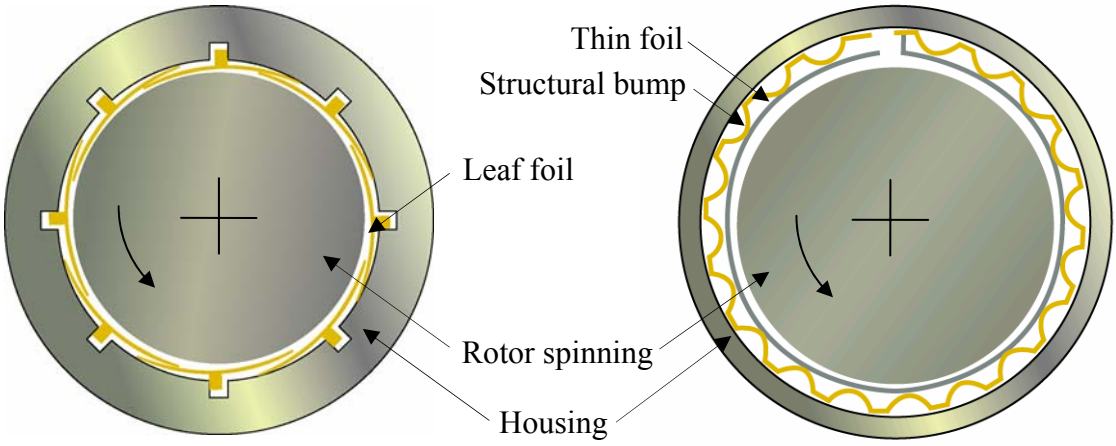

(a) Multiple leaf GFB **(b) Corrugated bump GFB**

Figure 1. Typical Gas Foil Bearings for oil-free turbomachinery

The published literature notes that multiple leaf GFBs are not the best of supports in high performance turbomachinery, primarily because of their inherently low load capacity [6]. A corrugated bump type GFB fulfills most of the requirements of highly

efficient oil-free turbomachinery, with demonstrated ultimate load capacity up to 680 kPa (100 psi) [7, 8].

The forced performance of a GFB depends upon the material properties and geometrical configuration of its support structure (the top foil and bump strip layers), as well as the hydrodynamic film pressure generated within the bearing clearance. In particular, the underlying support structure dominates the static and dynamic performance of high speed, heavily loaded GFBs [9]. For example, due to the elastic deflection of the bump strip layers, GFBs show relatively small changes in film thickness as compared to those in journal eccentricity. The GFB overall stiffness depends mainly on the softer support structure, rather than on that of the gas film, which "hardens" as the shaft speed and applied load increase. Material hysteresis and dry-friction dissipation mechanisms between the bumps and top foil, as well as between the bumps and the bearing inner surface, appear to enhance the bearing damping [10].

The envisioned application of GFBs into midsize gas turbine engines demands accurate performance predictions anchored to reliable test data. Modeling of GFBs is difficult due to the mechanical complexity of the bump-foil structure, further aggravated by the lack of simple, though physically realistic, energy dissipation models at the contact surfaces where dry-friction is prevalent.

In this report, the top foil, modeled as a structural shell using Finite Elements (FE), is integrated with the bump strip layers and in conjunction with the hydrodynamic gas film to predict the static and dynamic load performance of GFBs. Model predictions for two types of top foil structures, one and two dimensional, are compared to limited test results available in the literature. The effects of a mechanical preload on the GFB forced performance and stability characteristics are also studied. Shims installed under a bump strip layers at selected circumferential locations provide the preloads, thus modifying the nominal film thickness of the gas foil bearing. The objective is to determine enhancements in load capacity and rotordynamic instability for operation with small static loads and at high rotor speeds.

II. LITERATURE REVIEW

In 1953 Blok and van Rossum [11] introduce the concept of Foil Bearings (FBs). The authors point out that bearing film thickness, larger than that of rigid gas bearings, can improve operational reliability and provide a solution for problems related to the thermal expansion of both a journal and its bearing. Field experience has proved, since the late 1960's, that Gas Foil Bearings (GFBs) are far more reliable than ball bearings that were previously used in Air Cycle Machines (ACMs) installed in aircrafts. Therefore, GFBs have since been used in almost every new ACM installed in both civil and military aircraft [1]. This literature review discusses previous work related to the analysis of corrugated bump type GFBs.

Implementation of GFBs into high performance applications demands accuracy in modeling capabilities. Engineered GFBs must have a dimensionless load capacity larger than unity, i.e. specific pressure (W/LD) > P_a [2].

Heshmat et al. [9,12] first present analyses of bump type GFBs and detail the bearings static load performance. The predictive model couples the gas film hydrodynamic pressure generation to a local deflection (w_d) of the support bumps. In this simple of all models, the top foil is altogether neglected and the elastic displacement $w_d = \alpha\ (p\text{-}p_a)$ is proportional to the local pressure ($p\text{-}p_a$) and a structural compliance (α) coefficient which depends on the bump material, thickness and geometric configuration. This model, ubiquitous in the literature of GFBs, is hereby known as the *simple elastic foundation model*.

Peng and Carpino [13,14] present finite difference formulations to calculate the linearized stiffness and damping force coefficients of GFBs. The model includes both fluid (gas) film and structural bump layers used to simultaneously solve the Reynolds equations, and a simple equation to calculate iteratively gas film thickness for compliant GFBs. In the model of the underlying foil structure, a perfectly extensible foil is placed on top of the corrugated bumps. The model considers two neighboring bumps are not connected, i.e. no relative motion between them is assumed to occur.

Carpino et al. [15-17] have advanced the most complete computational models to date, including detailed descriptions of membrane and bending effects of the top foil, and accounting for the sub-foil structure elastic deformation. In [15,16], the authors build FE

models for the gas film and the foil structure, couple both models through the pressure field and get solutions using an iterative numerical scheme.

The bending and membrane rigidity terms of the FE model for the foil structure are not coupled so that the former and the latter render both the displacements for the bending plate and elastic plane (or membrane) models, respectively. On the other hand, [17] introduces a fully coupled finite element formulation for foil bearings. The FE formulations are based on moment, tension, curvature, and strain expressions for a cylindrical shell so that the membrane and bending stresses in the shell are coupled. This model incorporates both the pressure developed by the gas film flow and the structural deflections of the top and bump foils into a unique finite element. The predictions exhibit irregular shapes of pressure and film thickness due to foil detachment in the exit region of the gas film. Note that references [15-17] model the structural bump layers as a simple elastic foundation and do not present FE models to calculate the stiffness and damping coefficients of GFBs, but rather analyze GFBs at their steady state.

San Andrés [10] presents an analysis of the turbulent bulk-flow of a cryogenic liquid foil bearing (FB) for turbopump applications. The model uses an axially averaged pressure to couple the flow field to the structural bump deflection. The foil structure model consists of a complex structural stiffness with a structural loss factor arising from material hysteresis and dry-frictional effects between the bumps and top foil, and the bumps and the bearing's inner surface. The predictions show that the liquid oxygen FB reduces the undesirable cross-coupled stiffness coefficients and gets rid of potentially harmful half rotating frequency whirl. This paper reveals an important advantage of the FB that it has nearly uniform force coefficients and increasing damping coefficients at low excitation frequencies.

Kim and San Andrés [18] validate the simple elastic foundation model predictions in comparison with limited experimental test data in [19]. The model uses an axially averaged pressure enabling a journal to move beyond the nominal clearance when subjected to large static loads. The predictions demonstrate that a heavily loaded gas foil bearing may have journal eccentricities over three times greater than its nominal clearance. Predictions for film thickness and journal attitude angle for increasing static loads are in good agreement with test data for moderately to heavily loaded GFBs with journal eccentricities greater than the nominal clearance. In lightly loaded regions, there

are obvious discrepancies between predictions and test data because of the fabrication inaccuracy of test GFBs [19,20]. At the ultimate load condition, the predictions show a nearly constant GFB static stiffness, indifferent to rotor speed, and with magnitudes close to the underlying bump support stiffness determined in contact conditions without rotor spinning.

Lee et al. [21] present the effects of bump foil stiffness on the static and dynamic performance of foil journal bearings. To consider the deflection of a foil structure, the top foil is modeled as an elastic beam-like model and the bump is modeled as a linear spring. Predictions call for optimal bump stiffness magnitudes at specific rotor speeds to maximize the bearing load capacity. Furthermore, bump stiffness affects the GFB stability for operation at high rotor speeds.

High operating speeds of a rotor supported on GFBs lead to relatively stiffer gas films in relation to the stiffness of the support bumps. Thus, the overall stiffness of GFBs depends mainly on the sub-foil structure stiffness and the damping arising from material hysteresis and dry-friction effects at the contact surfaces between bumps and top foil and bumps and bearing casing. An accurate modeling of the sub-foil structure is necessary to advance a more realistic predictive tool for the performance of GFBs.

III. DESCRIPTION OF GAS FOIL BEARINGS

Gas foil bearings (GFBs) are compliant-surface hydrodynamic bearings that use ambient air or any process gas as the lubricating fluid. A hydrodynamic pressure builds up within the small gap or film between the rotating shaft and the smooth top foil. Figure 2 shows the configuration of a "first generation" bump type GFB [7]. The GFB consists of a thin (top) foil and a series of corrugated bump strip supports. The leading edge of the thin foil is welded to the bearing housing, and the foil trailing edge is free. Beneath the thin foil, a bump foil structure is laid on the inner surface of the bearing. The thin foil of smooth surface is supported by a series of bump foils acting as springs, thus making the bearing compliant. The bump strips provide a tunable structural stiffness [9]. Coulomb-type damping arises due to material hysteresis and dry-friction between the bumps and top foil, as well as between the bumps and the bearing inner surface [10].

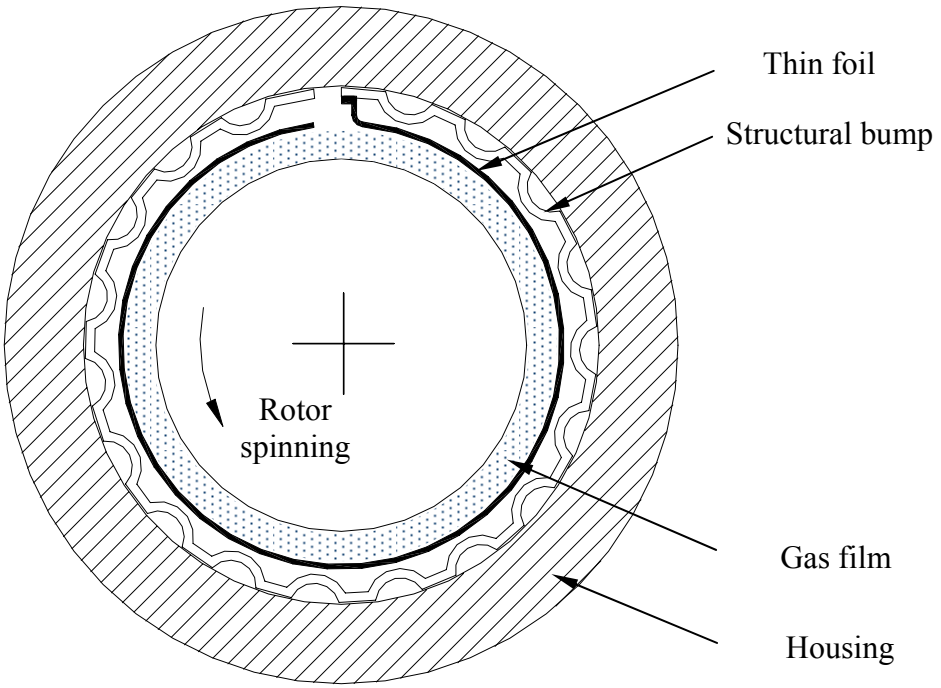

Figure 2. Schematic view of *first generation* bump type foil bearing

The Reynolds equation describes the generation of the gas pressure *(p)* within the film thickness *(h)*. For an isothermal, isoviscous ideal gas this equation is

$$\frac{\partial}{\partial x}\left(ph^3 \frac{\partial p}{\partial x}\right)+\frac{\partial}{\partial z}\left(ph^3 \frac{\partial p}{\partial z}\right)=6\mu\Omega R\frac{\partial(ph)}{\partial x}+12\mu\frac{\partial(ph)}{\partial t} \tag{1}$$

where (x, z) are the circumferential and axial coordinates on the plane of the bearing. The pressure takes ambient value (p_a) on the side boundaries of the bearing. The film thickness (h) for a perfectly aligned journal is

$$h = c - r_p \cos\left(\Theta - \Theta_p\right) + e_X \cos(\Theta) + e_Y \sin(\Theta) + w_d \tag{2}$$

where c and r_p are the assembled clearance and preload, respectively; and (e_X, e_Y) are the journal center displacements. w is the elastic deflection of the underlying support structure, a function of the hydrodynamic pressure field and the material and geometric characteristics of the support structure comprised of the top foil and the bump strip layers.

IV. MODELING OF FOIL SUPPORT STRUCTURE

IV.1 CONVENTIONAL SIMPLE ELASTIC FOUNDATION MODEL

Most published models for the elastic support structure in a GFB are based on the original work of Heshmat et al. [9,12]. This analysis relies on several assumptions which most researchers [10,13,14,18] also reproduce:

(1) The stiffness of a bump strip is uniformly distributed throughout the bearing surface, i.e. the bump strip is regarded as a uniform elastic foundation.

(2) A bump stiffness is constant, independent of the actual bump deflection, not related or constrained by adjacent bumps.

(3) The top foil does not to sag between adjacent bumps. The top foil does not have either bending or membrane stiffness, and its deflection follows that of the bump.

With these considerations, the local deflection of a bump (w_d) depends on the bump structural stiffness (K_f) and the average pressure (δp_A) across the bearing width, i.e.

$$w_d = \delta p_A / K_f \tag{3}$$

where $\delta p_A = \frac{1}{L}\int_0^L (p - p_a) dz$, and p_a is the ambient pressure beneath the foil.

Coupling of the simple model, Eq. (3), with the solution of Reynolds Eq. (1) is straightforward, leading to fast computational models for prediction of the static and dynamic force performance of GFBs, see [8-10] for example.

Presently, the simple foundation model is extended to account for and integrate with the elastic deformation of the top foil. The top foil is modeled as a flat shell, i.e. without curvature effects since the transverse deflections are roughly ~0.001 of the top foil assembled radius of curvature. Two structural models for the top foil follow:

a) <u>one-dimensional model</u> which considers an axially averaged gas film pressure acting along the top foil width and thus no structural deformation along the bearing axial direction; and,
b) <u>two-dimensional model</u> which considers the whole gas pressure field acting on the top foil with transverse deformations along the bearing circumferential and axial directions.

The first model is simpler and less computationally intensive. Both top foil strutucal models incorporate the bump strip layer as a series of linear springs, not connected with each other. Interactions between adjacent bumps are altogether neglected, as is usual in most predictive models. The stiffness of each bump is regarded as constant (irrespective of the load) does denoting no change in the nominal or manufactured bump pitch.

IV.2 ONE DIMENSIONAL ELASTIC MODEL FOR TOP FOIL

In their extensive GFB experimental work, Ruscitto et al. [19] report relatively small differences in axial gas film (minimum) thickness for heavily loaded conditions. This means that an average pressure causes a uniform elastic deformation along the top foil of width (L). Hence, a one dimensional structural model, with infinite stiffness along the bearing width, may suffice to model the top foil, as shown in Figure 3. One end of the top foil is fixed, i.e. with transverse deflection and rotation equal to nil; while the other end is

free. Figure 3 also shows the idealization of the 1D model with its degrees of freedom, namely transverse deflections (*w)* and rotations (ϕ).

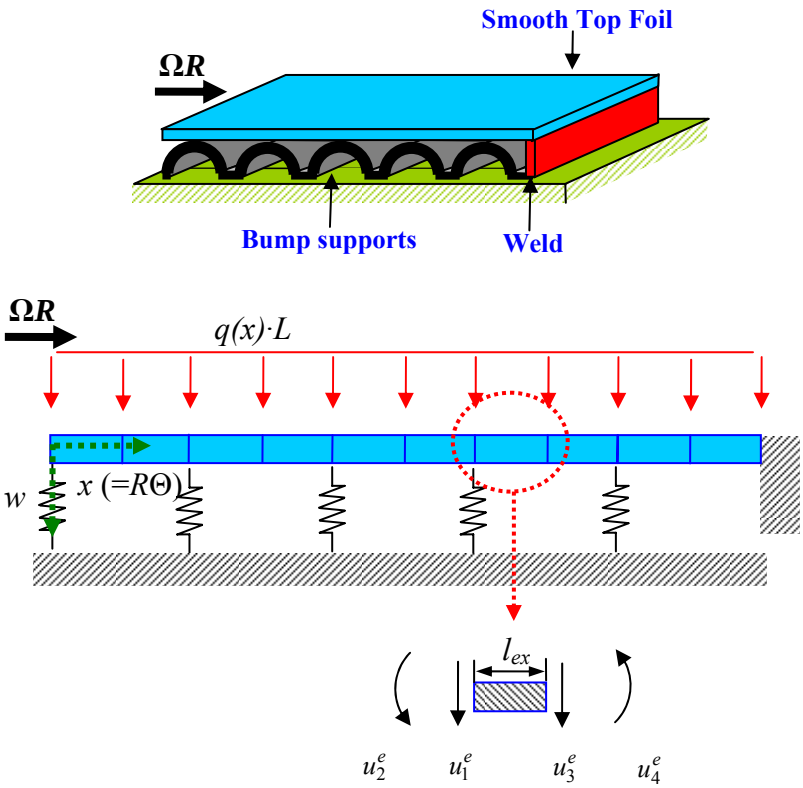

Figure 3. Configuration of top foil supported on a bump strip and its 1D structural model. Generalized displacements: $u_1^e = w_1$, $u_2^e = \phi_1$, $u_3^e = w_2$, **and** $u_4^e = \phi_2$

Figure 4 displays schematic representations of the actual and idealized structural deformations for the top foil and adjacent bumps. In actual operation, the bumps are flattened under the action of the acting pressure, the contact area with the top foil increases, and this effect increases locally the stiffness of the top foil. Hence, an anisotropic elastic model may compensate for the overestimation of top foil deflections between adjacent bumps. Presently, the elastic modulus for the top foil (E_t) is artificially increased, $E^* = E_t \times S_{fc}$, where (S_{fc}) as a stiffening factor in the circumferential direction. Note that the curvature radius of the top foil deflected shape (*sagging*) cannot exceed that of the original bumps shapes, thus suggesting the appropriate range of stiffening factors for known GFB configurations.

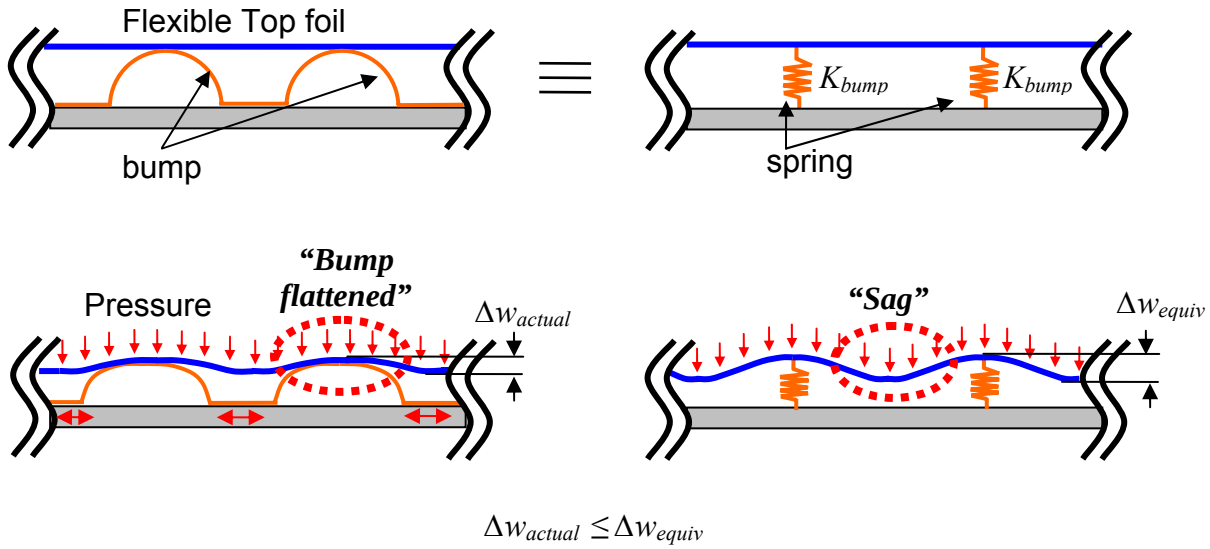

(a) Foil deflections in actual GFBs (b) Foil deflections for equivalent model

Figure 4. Schematic representations of deformations in actual and idealized top foil and bump strips

The top foil transverse deflection *(w)* along the circumferential axis (*x)* is governed by the fourth order differential equation:

$$\frac{d^2}{dx^2}\left(EI\frac{d^2w}{dx^2}\right) = q(x)\cdot L \tag{4}$$

where E and I are the elastic modulus and moment of inertia, and $q{\cdot}L=(p\text{-}p_a)\cdot L$ is the distributed load per unit circumferential length. Note that Eq. (4) is the typical formulation for the deflections of an *Euler-like* beam. Appendix A and reference [22] detail the weak form of Eq. (4) when integrated over the domain of one finite element.

IV.3 TWO DIMENSIONAL MODEL FOR TOP FOIL

The second model regards the top foil as a two dimensional flat shell supported on axially distributed linear springs located at every bump pitch, as shown in Figure 5. Figure 6, graphs (a) and (b), depicts the membrane force (N), shear force (Q) and bending moment (M) per unit element length, and external pressure difference ($q=p\text{-}p_a$) acting on

the shell element OABC. The generic displacements are denoted as *u, v* and *w* along the *x, y* and *z* directions, respectively [23].

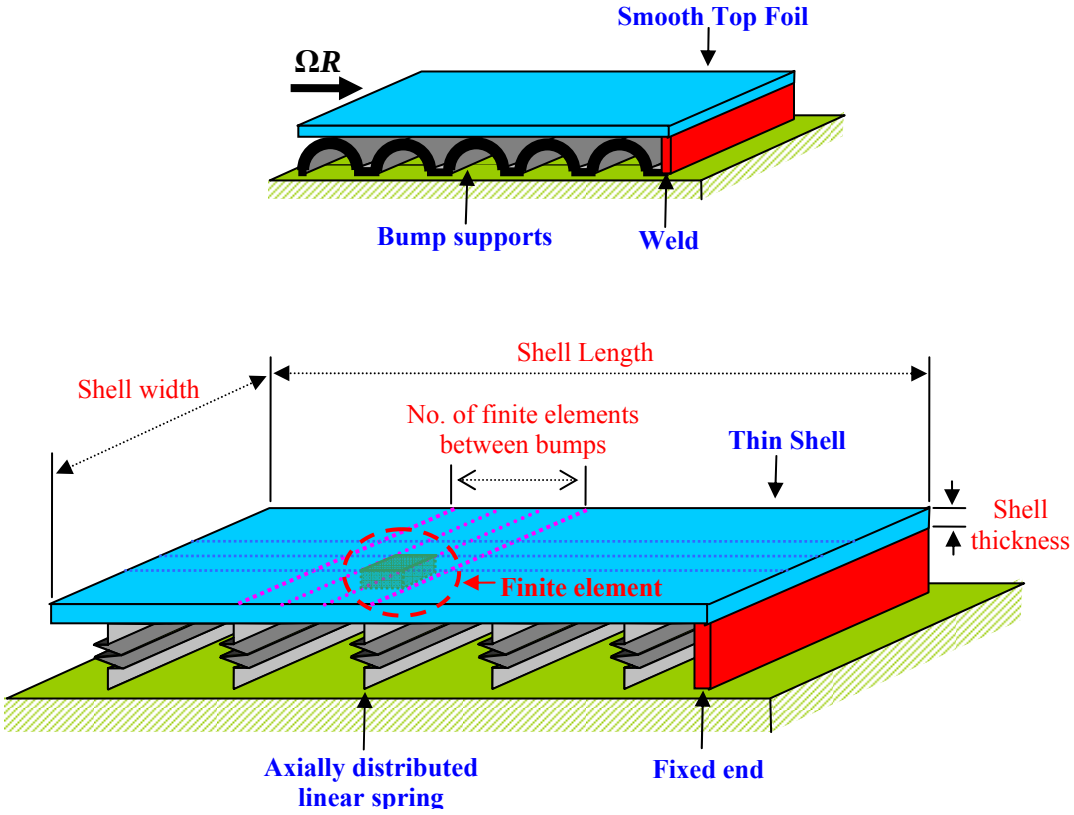

Figure 5. Configuration of top foil supported on a bump strip and its 2D structural model

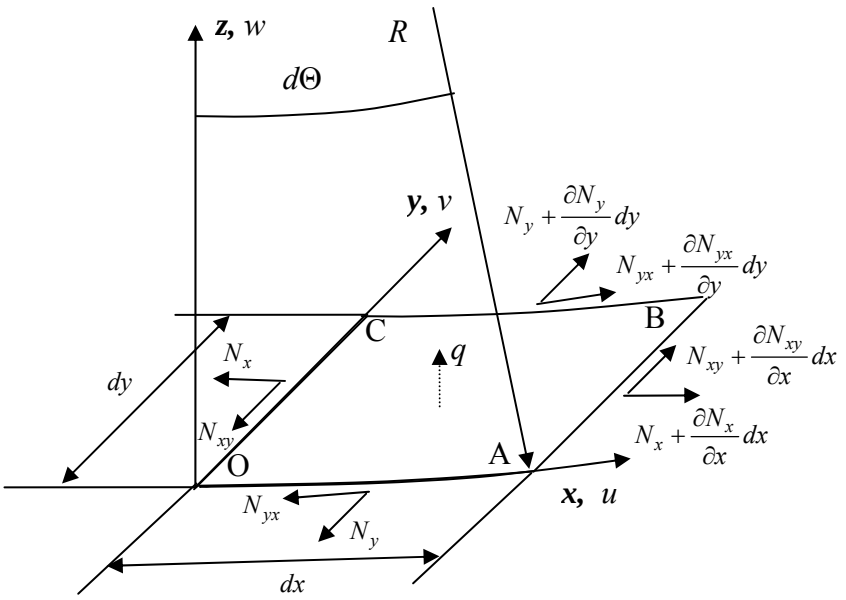

(a) Normal plane (membrane) stresses

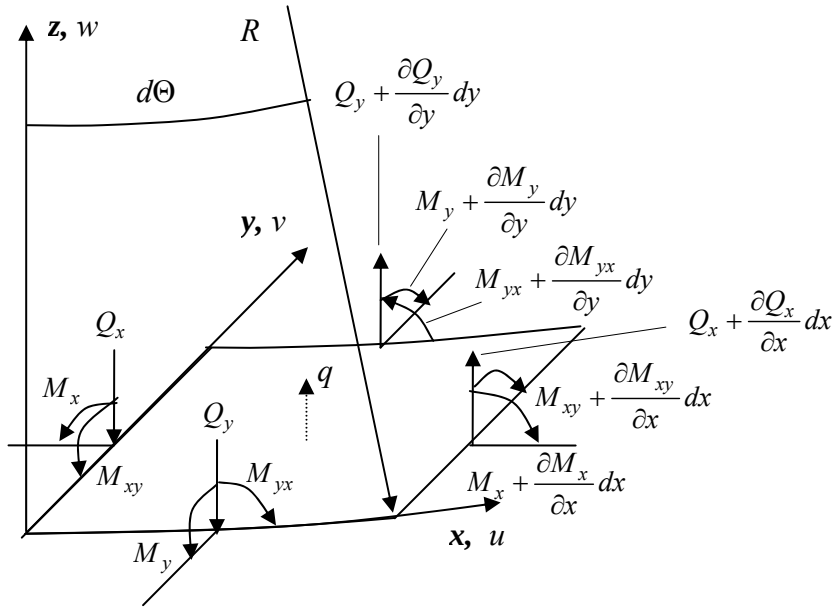

(b) Bending and shear stresses

Figure 6. Resultant membrane forces and bending moments per unit shell element length for a distributed load in the domain of a shell finite element

Timoshenko and Woinowsky-Krieger [23] detail the differential equations for the general cases of deformation in a cylindrical shell. In the present structural configuration, membrane or in-plane forces per unit element length (*N*) are negligible since the axial (side) ends of the top foil are regarded as free (not constrained) and because the gas film pressure acts normal to the top foil. Gas film shear forces between the film and top foil

and dry-friction forces between the top foil and bumps underneath do induce membrane forces. However, these are neglected for simplicity.

Presently, an anisotropic shell model will compensate the simplification. A stiffening factor (S_{fa}) for the top foil elastic modulus (E_t), i.e. $E_t^* = E_t \times S_{fa}$, in the axial direction and a stiffening factor (S_{fc}) in the circumferential direction will prevent the overestimation of the top foil deflections near the foil unconstrained (free) edges and between adjacent discrete bump structures, respectively. The stiffening factors are determined by trial and error!

Thus, the present analysis retakes the anisotropic, shear deformable plate model based on first-order shear deformation theory. As given in [22], the governing equations are

$$\begin{aligned} &\frac{\partial Q_x}{\partial x}+\frac{\partial Q_y}{\partial y}-q=0\,; \\ &\frac{\partial M_x}{\partial x}+\frac{\partial M_{yx}}{\partial y}-Q_x=0\,; \\ &\frac{\partial M_{yx}}{\partial x}+\frac{\partial M_y}{\partial y}-Q_y=0 \end{aligned} \tag{5}$$

where

$$\begin{aligned} &M_x=D_{11}\frac{\partial \phi_x}{\partial x}+D_{12}\frac{\partial \phi_y}{\partial x}\,;\; M_y=D_{12}\frac{\partial \phi_x}{\partial x}+D_{22}\frac{\partial \phi_y}{\partial y}\,;\; M_{xy}=D_{66}\left(\frac{\partial \phi_x}{\partial y}+\frac{\partial \phi_y}{\partial x}\right) \\ &Q_x=A_{55}\left(\phi_x+\frac{\partial w}{\partial x}\right);\;\; Q_y=A_{44}\left(\phi_y+\frac{\partial w}{\partial y}\right) \end{aligned} \tag{6}$$

and

$$\begin{aligned} &D_{11}=\frac{E_1 h_t^3}{12\left(1-\nu_{12}\nu_{21}\right)};\;\; D_{12}=\frac{\nu_{12}E_2 h_t^3}{12\left(1-\nu_{12}\nu_{21}\right)};\;\; D_{22}=\frac{E_2 h_t^3}{12\left(1-\nu_{12}\nu_{21}\right)};\;\; D_{66}=\frac{E_{12} h_t^3}{24\left(1-\nu_{12}\nu_{21}\right)} \\ &A_{55}=k_t\frac{E_{13}h_t}{2\left(1-\nu_{13}\right)};\quad A_{44}=k_t\frac{E_{23}h_t}{2\left(1-\nu_{23}\right)} \end{aligned} \tag{7}$$

ϕ_x and ϕ_y in Eq. (6) denote rotation angles about the y and x axes, respectively. h_t, E_{ij}, ν_{ij}, in Eq. (7) represent the shell thickness, anisotropic elastic modulii and Poisson's ratios, respectively [24]. k_t (=5/6) is a shear correction coefficient, introduced to account for the discrepancy between the distribution of transverse shear stresses of the first-order theory and actual distribution [22].

Note that, in Eqs. (5-7), neglecting the deflections (w, ϕ_y) along the y axis leads to the governing equations for Timoshenko's beam theory [23]. Appendix B details the weak form of Eqs. (5-7) when integrated over a two-dimensional finite element domain.

Figure 7 presents a four-node, shell element supported on an axially distributed linear spring on one end, as taken from Fig. 5. l_{ex}, l_{ey}, and h_t represent the element length, width, and thickness, respectively. At each node, there are three degrees of freedom, a transverse deflection and two rotations. Note that the axially distributed linear spring reacts only to the transverse deflection, w.

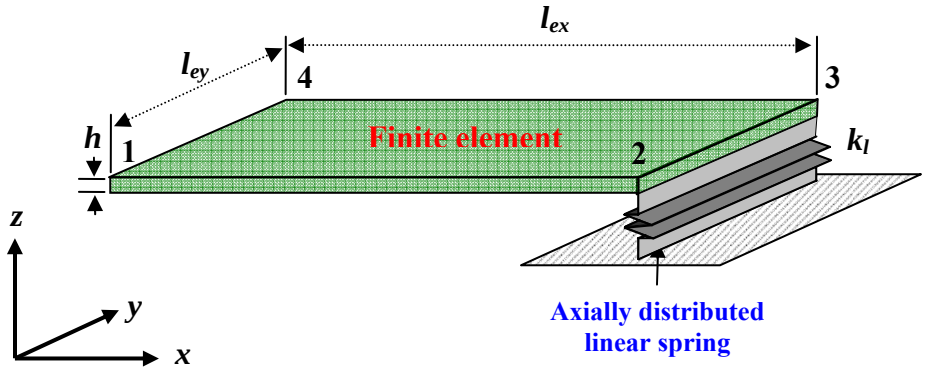

Figure 7. Four-node, shell finite element supported on an axially distributed linear spring

Equation (8) below details the stiffness matrix [K^s] for one structural bump supporting a top foil at one of its edges. This matrix is integrated into the shell element stiffness matrix [K^e] given in Appendix B.

$$\left[K^s\right]=\frac{K_l}{3}\begin{bmatrix}0&0&0&0&0&0&0&0&0&0&0&0\\0&0&0&0&0&0&0&0&0&0&0&0\\0&0&0&0&0&0&0&0&0&0&0&0\\0&0&0&1&0&0&1/2&0&0&0&0&0\\0&0&0&0&0&0&0&0&0&0&0&0\\0&0&0&0&0&0&0&0&0&0&0&0\\0&0&0&1/2&0&0&1&0&0&0&0&0\\0&0&0&0&0&0&0&0&0&0&0&0\\0&0&0&0&0&0&0&0&0&0&0&0\\0&0&0&0&0&0&0&0&0&0&0&0\\0&0&0&0&0&0&0&0&0&0&0&0\\0&0&0&0&0&0&0&0&0&0&0&0\end{bmatrix} \quad \text{for} \quad \left\{U^e\right\}=\begin{Bmatrix}w_1\\\phi_{x1}\\\phi_{y1}\\w_2\\\phi_{x2}\\\phi_{y2}\\w_3\\\phi_{x3}\\\phi_{y3}\\w_4\\\phi_{x4}\\\phi_{y4}\end{Bmatrix} \tag{8}$$

where $K_l = K_f \times s_0 \times l_{ey}$; s_0 is the bump pitch and K_f, the bump stiffness per unit area, is

estimated using Iordanoff's [25] analytical expressions for a bump with both sides free, or one end free and the other fixed. Although the formulas in [25] include provisions for a dry friction coefficient, at present none is being used. Note that when considering the dynamic behavior of a bump support, a complex stiffness, $K_f' = K_f(1+i\gamma)$, is easily defined to account for a material loss factor (γ) arising from hysteresis and dry-friction.

Adding the bump stiffness matrix [K^s] at the appropriate locations while assembling the shell element stiffness matrices [K^e] by using a connectivity array leads to a global stiffness matrix $[K^G] = \bigcup\left\{\left[K^e\right]+\left[K^s\right]\right\}$. The global stiffness matrix [K^G] is reduced by considering the geometric constraints, $w = \phi_x = \phi_y = 0$, along the top foil fixed end.

Without journal misalignment, the pressure field is symmetric about the bearing mid plane. In this case, the FE procedure models only one half side of the top foil and support bumps, thus reducing computational costs significantly.

The global system of equations for deflections of the top foil and bump supports is given by

$$\left[K^G\right]\left\{U^G\right\} = \left\{F^G\right\} \tag{9}$$

where [K^G] is a symmetric, positive definite matrix, $\{U^G\}$ is the vector of generalized deflections (transverse displacements and rotations), and $\{F^G\}$ is the vector of generalized forces, namely pressures acting on the top foil.

Prior to computations coupling the structure deflections to the thin film gas flow governed by Reynolds Eq. (1), the global stiffness matrix, derived from the 1D and 2D FE models, is decomposed using Cholesky's procedure [26], i.e.

$$\left[L\right]\left[L^T\right] = \left[K^G\right] \tag{10}$$

Note that the FE structural model analysis is performed off-line. In this manner, the computational efficiency of the numerical scheme is greatly enhanced.

Numerical solution of Eq. (9), using the decomposition, is quite fast since it involves two procedures, first a forward substitution solving $[L]\{x\}=\{F^G\}$, and next a backward substitution solving $[L]^{\mathrm{T}}\{U^G\}=\{x\}$. The transverse deflection field (w) is extracted from $\{U^G\}$ and used to update the film thickness for solution of Reynolds equation within the framework of an iterative scheme.

V. COMPARISONS OF PREDICTIONS TO PUBLISHED TEST DATA

V. 1 CONFIGURATION OF TEST GFB

The validity of the analysis and computational program is assessed by comparison of predictions to experimental data available in the open literature. Table 1 provides parameters for the test foil bearing given in [19] and Figure 8 depicts the configuration of the bump foil strip. The foil bearing is a "first generation" type with one 360º top foil and one bump strip layer, both made of Inconel X-750. The top foil and bump layer are spot welded at one end to the bearing sleeve. The other end of the top foil is free as well as the end of the bump strip layer. The journal rotational direction is from the free end of the top foil towards its fixed end.

Table 1 Design details of foil bearing, reference [19]

Bearing radius, $R=D/2$	19.05 mm	(0.75 inch)
Bearing length, L	38.1 mm	(1.5 inch)
Foil arc circumferential length, l_x	120 mm	(4.7 inch)
Radial journal travel, c_J (~ clearance)	31.8 μm	(1.25 mil)
Top foil thickness, t_t	101.6 μm	(4 mil)
Bump foil thickness, t_b	101.6 μm	(4 mil)
Bump pitch, s	4.572 mm	(0.18 inch)
Half bump length, l_0	1.778 mm	(0.07 inch)
Bump height, h_b	0.508 mm	(0.02 inch)
Number of bumps*, N_b	26	
Bump foil Young's modulus, E	214 Gpa	(31 Mpsi)
Bump foil Poisson's ratio, v	0.29	

All tests in [19] were performed with air at ambient condition. Because the bearing clearance for the test bearing was unknown, the journal radial travel (c_J) was measured by performing a static load-bump deflection test. Details of the measuring procedure are described in [19]. The journal radial travel refers to the displacement where the journal

* The number of bumps (N_b) is calculated by dividing the foil arc circumferential length (l_x) by the bump pitch (s).

can sway under an arbitrary static load condition[†]. Hence, in [19], the journal radial travel ($2c_J$ =63.6 μm) is obtained from the total displacement of the bearing when a 0.9 kg (2 lb) load was applied first downward, and then upwards.

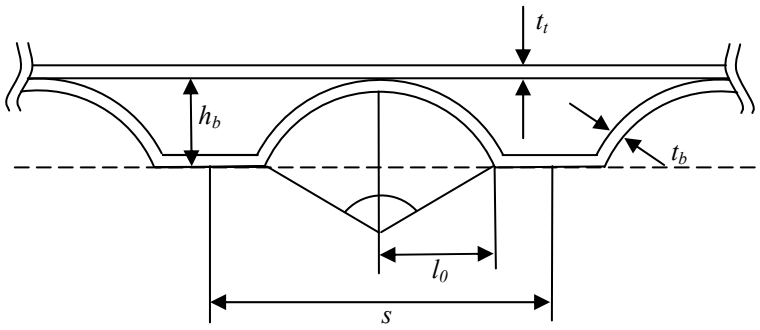

Figure 8. Configuration of top foil and bump foil strips

The structural stiffness per unit area (K_f) is estimated from Iordanoff's formulae [25]. The bump pitch (s) is regarded as constant and the interaction between bumps is neglected. The calculated structural stiffness coefficients per unit area for a free-free ends bump and a fixed-free end bump are K_{ff} = 4.7 GN/m^3 and K_{fw} = 10.4 GN/m^3, respectively.

V.2 MINIMUM FIILM THICKNESS AND JOURNAL ATTITUDE ANGLE

The GFB computational tools integrating the 1D and 2D finite element top foil structural models, as well as the earlier simple elastic foundation model, predict the static and dynamic force performance of the test GFB.

The 2D FE model uses a mesh of 78 and 10 elements in the circumferential and axial directions, respectively. The same mesh size is used for the finite difference numerical scheme solving Reynolds Eq. and calculating the hydrodynamic gas film pressure. On the other hand, the 1D FE model uses a mesh of 78 elements in the circumferential direction. A mesh of 78 and 10 elements, in the circumferential and axial directions, respectively, is used to analyze the gas film pressure. Predictions using the simple elastic foundation model, for a mesh of 90 and 10 elements in the circumferential and axial directions, respectively, are directly taken from [18].

[†] This ad-hoc procedure reveals the region where the foil structure is apparently very "soft."

Top foil stiffening factors S_{fc}= 4 and S_{fa}= 1 in the circumferential and axial directions, respectively, were obtained through parametric studies based on the recorded test data in [19]. In the 2D FE model, foil deflections along its edges are calculated using the axial upstream pressures modified by the local Peclet number [27], a procedure based on physical reasoning which improves the accuracy in the prediction in the gas film thickness. Note that FE predictions underestimate the top foil deflections when compared to the test data in [19]. This behavior is caused by the omission of membrane stresses in the current model.

Figure 9 presents the minimum film thickness versus applied static load for operation at shaft speeds equal to (a) 45,000 rpm and (b) 30,000 rpm. The graphs includes the test data [19], and predictions for three increasingly complex structural models; namely, the simple elastic foundation, 1D top foil acted upon an axially averaged gas pressure, and the 2D top foil with circumferential stiffening. In the tests, film thicknesses were recorded at both the bearing mid-plane and near the bearing exit-planes, i.e. 1.6 mm from the bearing axial ends. The 2D model predictions show minimum film thicknesses along the bearing mid-plane and near the bearing edges, i.e. 1.9 mm away. Both the simple elastic model and the 1D FE model predictions show a film thickness not varying across the bearing width since the models rely on an axially averaged pressure field.

In general, all model predictions agree fairly with the test data [19]. Incidentally, the measurement errors reported in [19] render a precision uncertainty of ~15 % for film thickness.

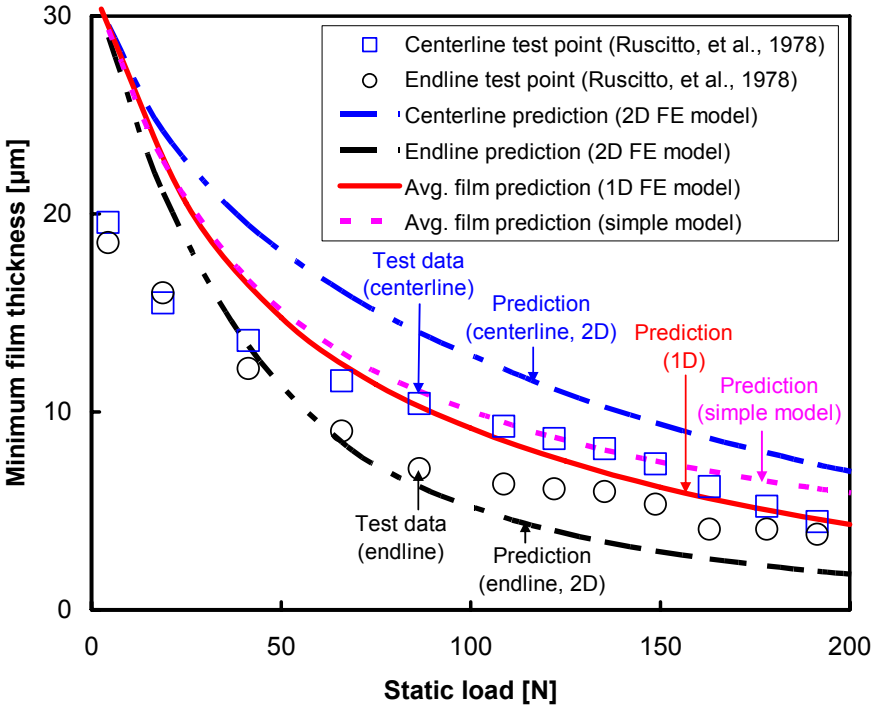

(a) 45,000 rpm

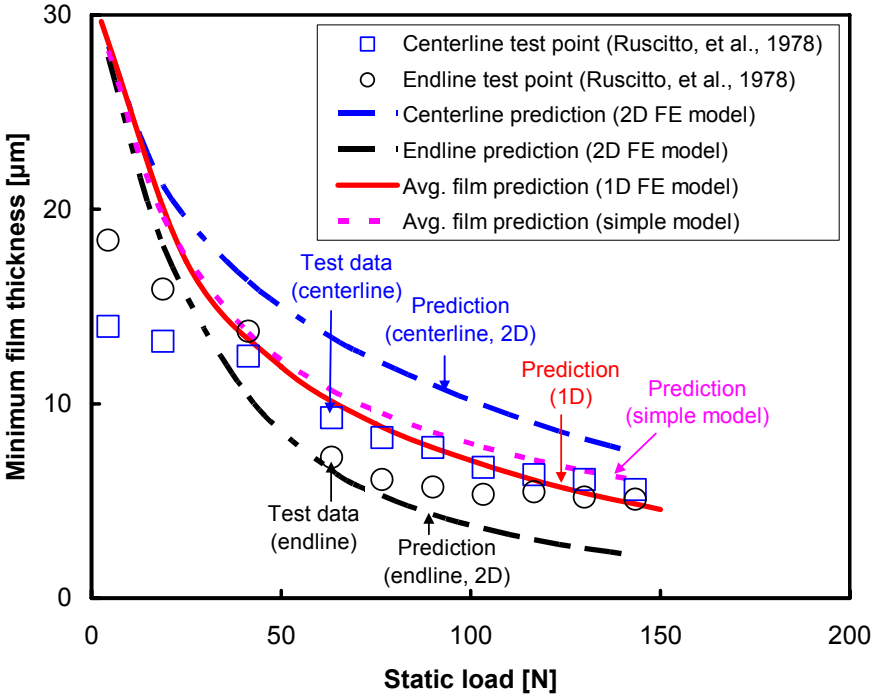

(b) 30,000 rpm

Figure 9. Minimum film thickness versus static load. Predictions from three foil structural models and test data [19]

Over the whole range of static loads, 2D top foil model predictions overestimate the minimum film thickness at the bearing mid-plane, and slightly underestimate this parameter at the top foil edge. The discrepancies are due to membrane forces preventing the extension of the top foil. Membrane forces force a uniform deflection along the bearing width, in particular for heavy static loads. This effect is most notable for a uniform pressure field along the bearing width. See Fig. 10 for a comparison of the axially averaged minimum film thickness calculated from the 2D model and the test data (simple arithmetic average of film thicknesses recorded at the bearing mid-plane and near edges). The predictions correlate very well with the test data at 45,000 rpm and 30,000 rpm, respectively.

The assumption of an axially uniform minimum film thickness in the 1D top foil model results in a significant reduction of computational costs, as discussed in more detail later. More importantly, the 1D top foil model predictions show the best correlation to the collected experimental results. The simpler model predictions slightly overestimate the minimum film thickness, especially for heavy static loads.

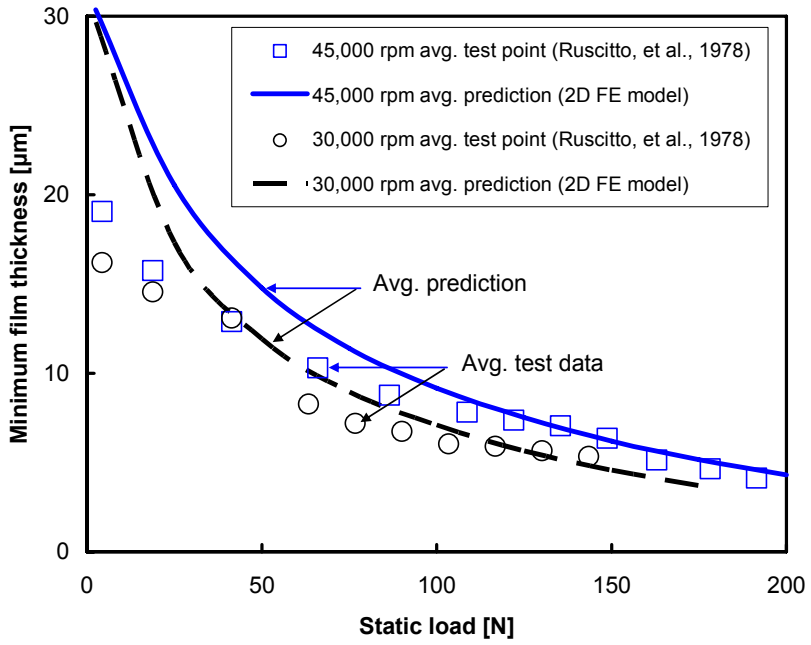

Figure 10. Axially averaged minimum film thickness versus static load. Predictions from 2D top foil model and test data [19]

Figure 11 depicts the journal attitude angle versus applied static load for speeds equal to (a) 45,000 rpm and (b) 30,000 rpm, respectively. The graph includes predictions from

the three structural models and test data [19]. All model predictions slightly underestimate the test data above 60 N. The notable discrepancy between predictions and test results for static loads below 60 N can be attributed to foil bearing fabrication inaccuracy [19]. The 1D top foil structural model predictions demonstrate the best correlation to the test data. In general, all model predictions agree well with the test data.

Figure 12 presents the predicted journal eccentricity versus applied static load for operation at a rotational speed of 45,000 rpm. Reference [19] does not provide test data regarding journal eccentricity. For static loads above 60N, i.e. specific load of 41.4 kPa (6 psi), where the journal eccentricity exceeds the nominal clearance (c_J), the journal displacement is proportional to the applied load. The simple elastic foundation model predicts an ultimate static stiffness K_G=5.2×10^6 N/m, which is nearly identical to the structural stiffness K_S=5.3×10^6 N/m. See [18] for a comparison of the journal eccentricity predicted using the simple model to the structural deflection for load contact without journal spinning. Similar trends in predicated journal eccentricity are evident for the 1D and 2D top foil structural models. However, for heavy static loads, the 2D top foil model shows a slightly larger eccentricity since the top foil, being flexible, "sags" in between adjacent bumps.

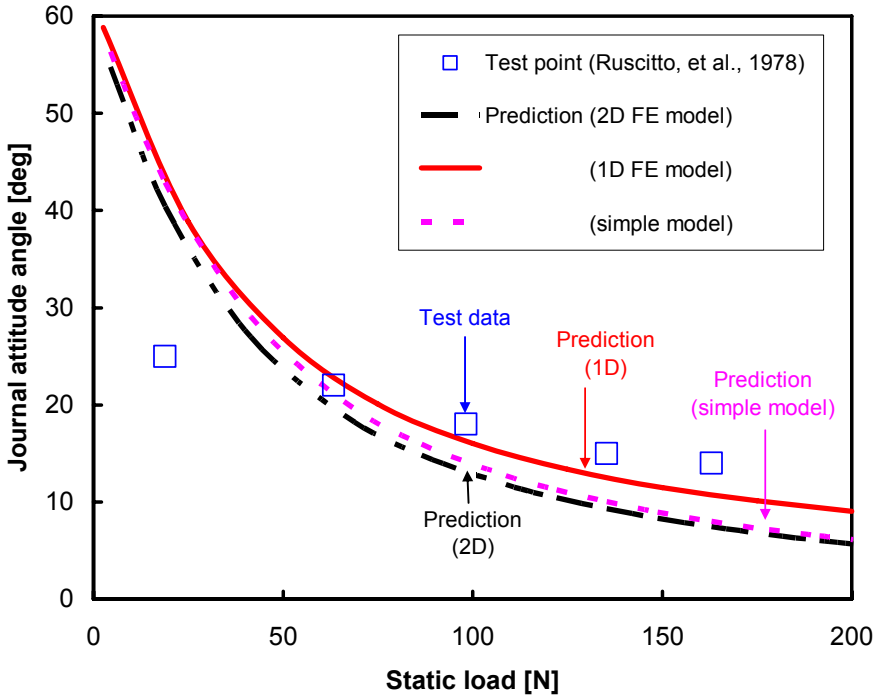

(a) 45,000 rpm

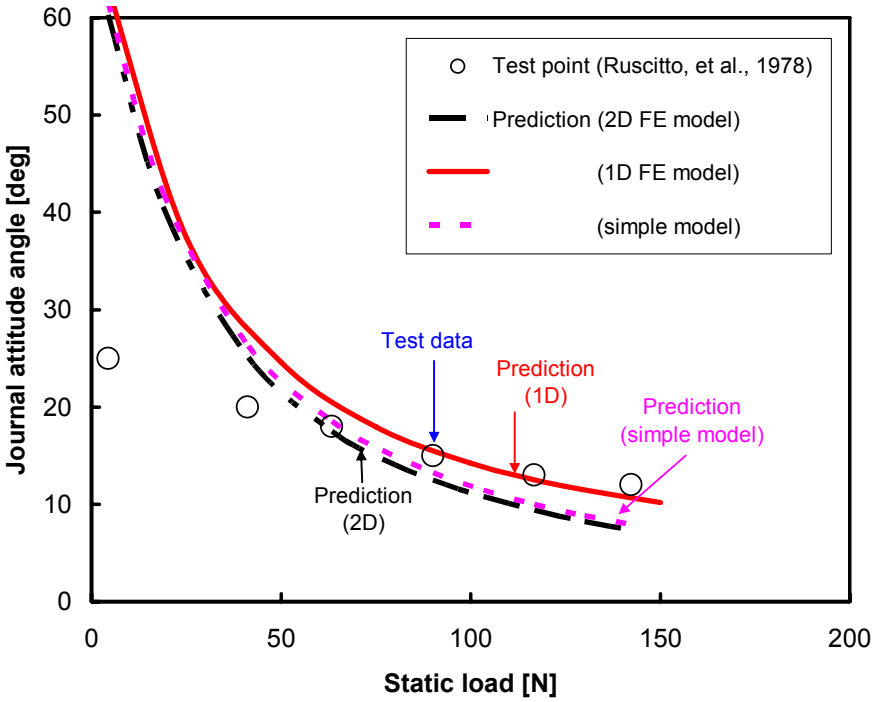

(b) 30,000 rpm

Figure 11. Journal attitude angle versus static load. Predictions from three foil structural models and test data [19]

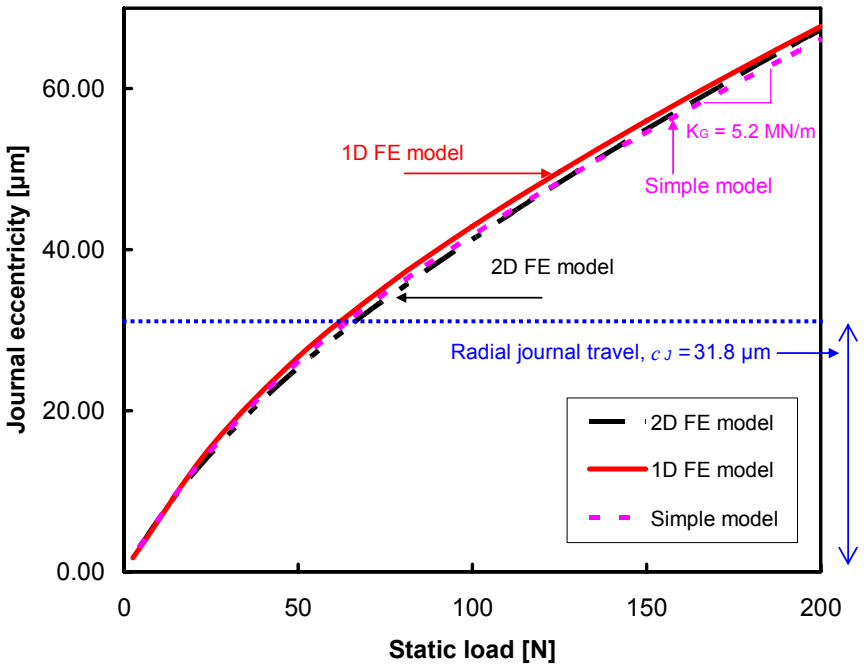

Figure 12. Journal eccentricity versus static load at 45 krpm, Predictions from three foil structural models for GFB in [19]

Figure 13 displays the predicted dimensionless pressure field (p/p_a) and the corresponding film thickness derived from the 2D top foil structural model. A static load of 200 N, specific pressure = 138 kPa (20 psi), acts on the rotor operating at a speed of 45,000 rpm. The hydrodynamic film pressure builds up within the smallest film thickness region. During operation, the top foil could detach, not allowing for sub-ambient pressures, i.e. $p \geq p_a$. For the heavily loaded condition (200 N) and due to the bearing inherent compliance, the model prediction shows a large circumferential region of uniform minimum film. The film thickness is nearly constant along the bearing axial length except near the axial edges, as in the experiments [19]. The softness of the top foil in between individual bumps, as shown in the film thickness field causes the local pressure field to sag between consecutive bumps, i.e. the appearance of a "*ripple*" like effect.

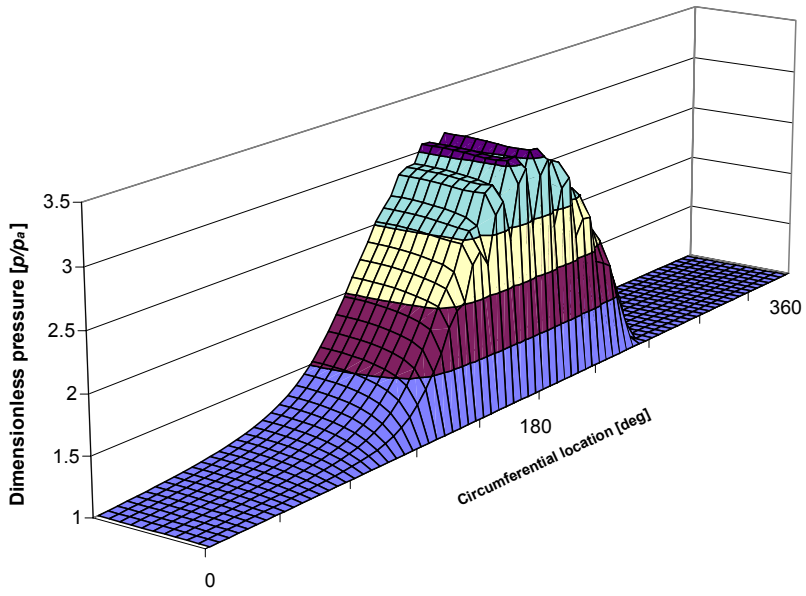

(a) Pressure field

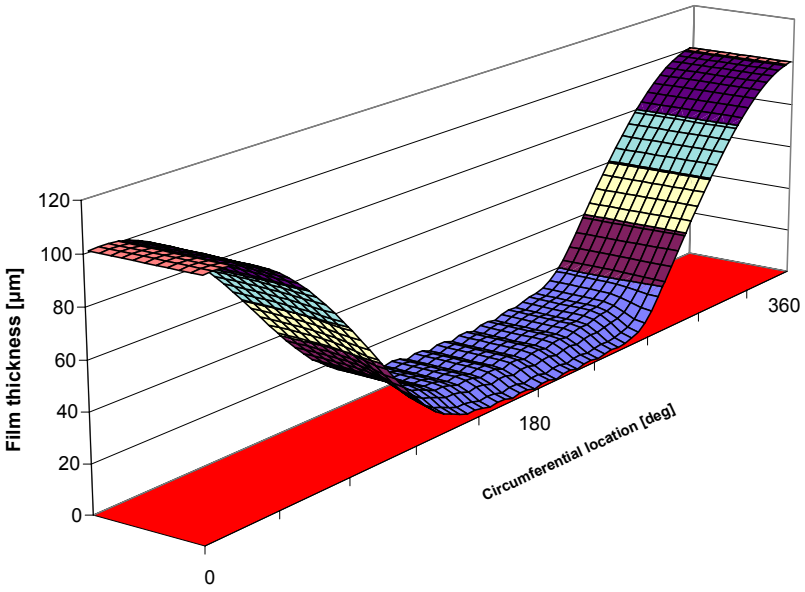

(b) Film thickness field

Figure 13. Predicted (a) dimensionless pressure field and (b) film thickness field from 2D top foil structural model. Static load: 200 N, rotor speed: 45 krpm. Bearing configuration given in [19]

Figure 14 presents the predicted film thickness versus circumferential location for the 1D top foil model and the measured film thickness [19] for a static load of 134.1 N and rotor speed of 30 krpm. Along the zone of smallest film thickness, the predictions match very well with the test data. Recall that the model does not account for the interaction between adjacent bumps, thus showing a slight difference in the pitch of the *ripple* shapes. Note that the test GFB has a nearly constant film thickness along the bearing axial length (Δh < 1μm) for both load and speed conditions, as shown in Fig 9 (b).

Although the test GFB has a largely unknown radial clearance, due to a fabrication inaccuracy, and its nominal bearing clearance is experimentally determined through a simple load-deflection test, the comparisons demonstrate a remarkable correlation between predictions and test data in the region of minute, nearly uniform, film thickness. These comparisons validate the 1D top foil model for accurate prediction of GFB static load performance.

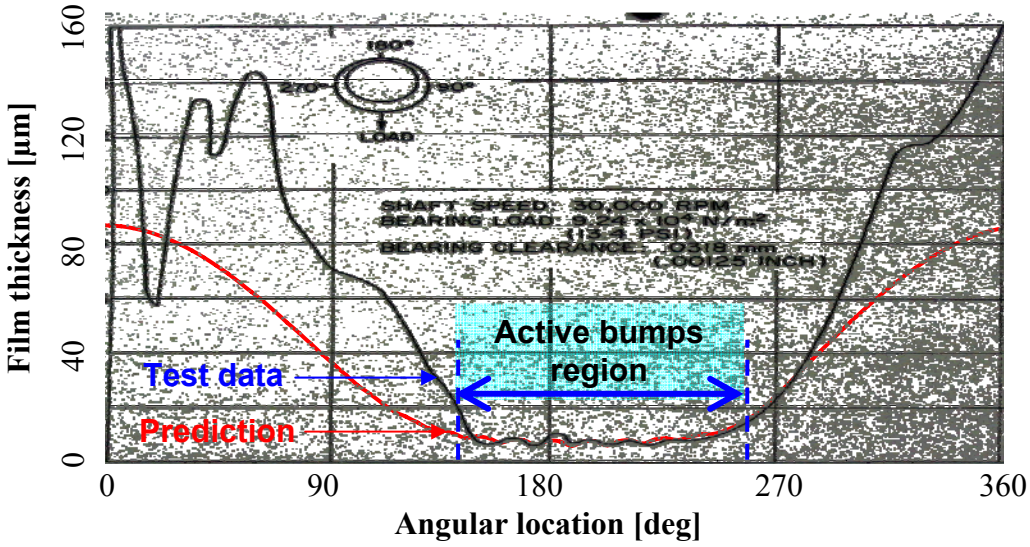

Figure 14. Film thickness versus angular location at bearing mid-plane. Prediction from 1D top foil model and test data [19]. Static load: 134.1 N. Rotor speed: 30 krpm

V. 3 PREDICTED STIFFNESS AND DAMPING FORCE COEFFICEINTS

To date there is no published experimental data on GFB force coefficients, stiffness and damping.

Figure 15 displays the bearing stiffness coefficients versus excitation frequency as determined by the three structural support models. A static load of 150 N, i.e. specific load of 1 bar (15 psi), is applied at 45,000 rpm. Synchronous excitation corresponds to a frequency of 750 Hz. The results correspond to a negligible structural loss factor, $\gamma = 0.0$, known to have an insignificant effect on the direct stiffness coefficients [10]. The direct stiffness coefficients (K_{XX}, K_{YY}) increase with excitation frequency due to the "hardening" of the gas film. All models predict very similar direct stiffness coefficients.

The simple elastic foundation model predicts the largest direct stiffness, K_{XX}, while the 2D top foil model renders the smallest. The *"sagging"* effect of the top foil in between adjacent bumps in the 1D and 2D FE models is thought to reduce slightly the bearing stiffness K_{XX}. All predictions of cross-coupled stiffness coefficients show positive values. Note that cross-coupled stiffness coefficients with same sign do not have destabilizing effects [28]. The 1D top foil model predicts the largest K_{XY} and the smallest K_{YX}. The 2D model predicts the smallest K_{XY}, while the simple model predicts the largest K_{YX}. All model predictions demonstrate much greater direct stiffnesses, K_{XX} and K_{XX}, than cross-coupled stiffnesses, K_{XY} and K_{YX}. Note that the difference in vertical axis scales in Figure 15(a-c).

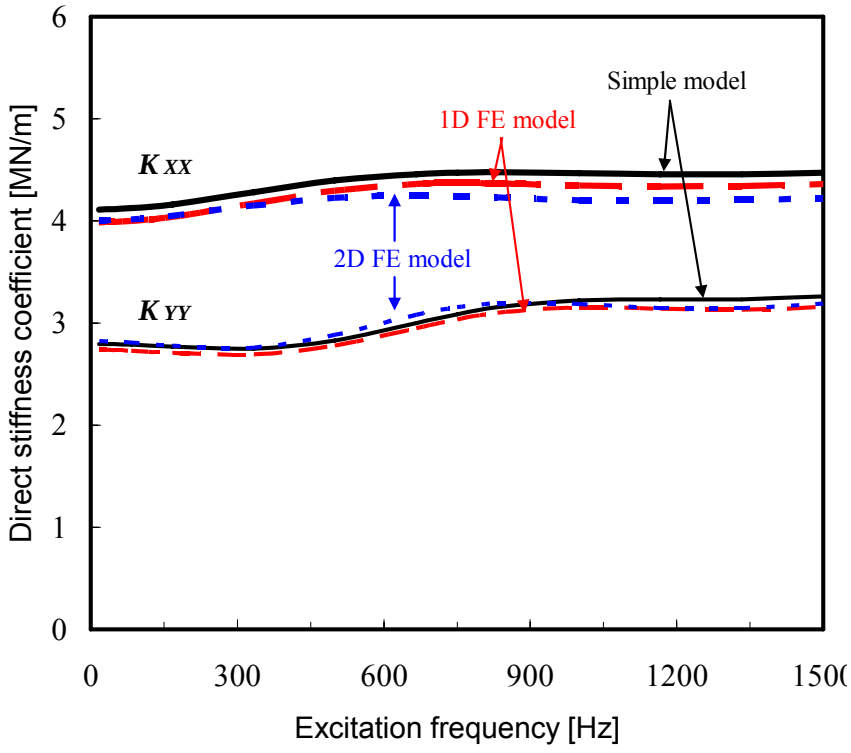

(a) K_{XX}, K_{YY}

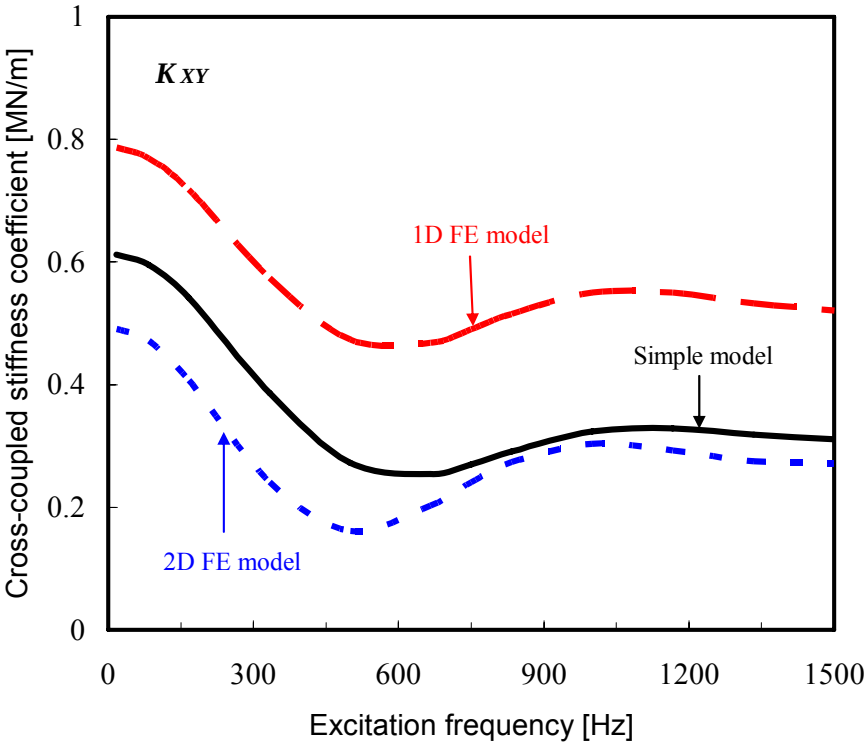

(b) K_{XY}

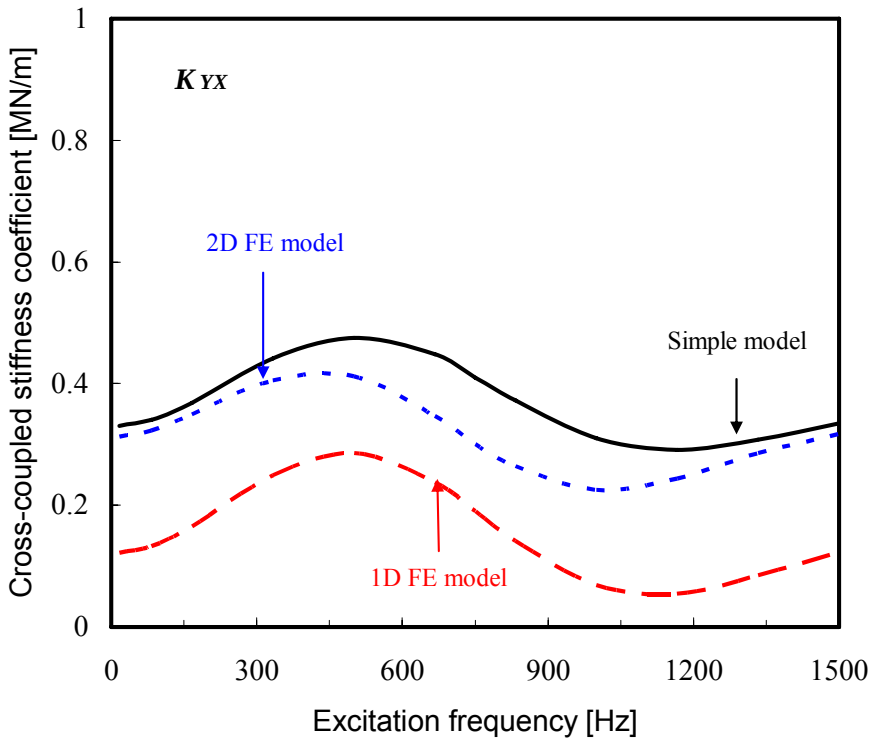

(c) K_{YX}

Figure 15. Predicted GFB stiffness coefficients versus excitation frequency for three structural models. Rotor speed: 45 krpm, Static load: 150 N. Structural loss factor γ = 0.0.

Figure 16 displays predicted damping coefficients versus excitation frequency as determined from the three structural models. Static load and rotor speed are as in the last figure. The structural loss factor γ = 0.4 represents a hysteresis damping effect in the bump strip layer. With a structural loss factor (γ = 0.4), the direct damping coefficients (C_{XX}, C_{YY}) increase significantly when compared to those for γ = 0.0, i.e. without material damping. Regardless of the structural loss factor, the 2D top foil model predicts the smallest direct damping coefficients (C_{XX}, C_{YY}). The simple elastic foundation model prediction shows the largest coefficients, except for excitation frequencies lower than 500 Hz, where the 1D FE model predicts the largest C_{XX} and C_{YY} for a null loss factor (γ = 0). Predictions of cross-coupled damping coefficients, C_{XY} and C_{YX}, do not show a discernible difference among the three models. Generally, cross-coupled damping coefficients (C_{XY}, C_{YX}) decrease in magnitude as the excitation frequency increases. Note that the vertical axes of Figs. 16 (a) and 16 (b) show a log scale, while Figs. 16 (c) and 16 (d) show a linear scale along the vertical axes.

All model predictions demonstrate much greater direct damping, C_{XX} and C_{XX}, than cross-coupled damping, C_{XY} and C_{YX}. In particular, for γ = 0.4, note the rapid reduction in direct damping as the excitation frequency increases.

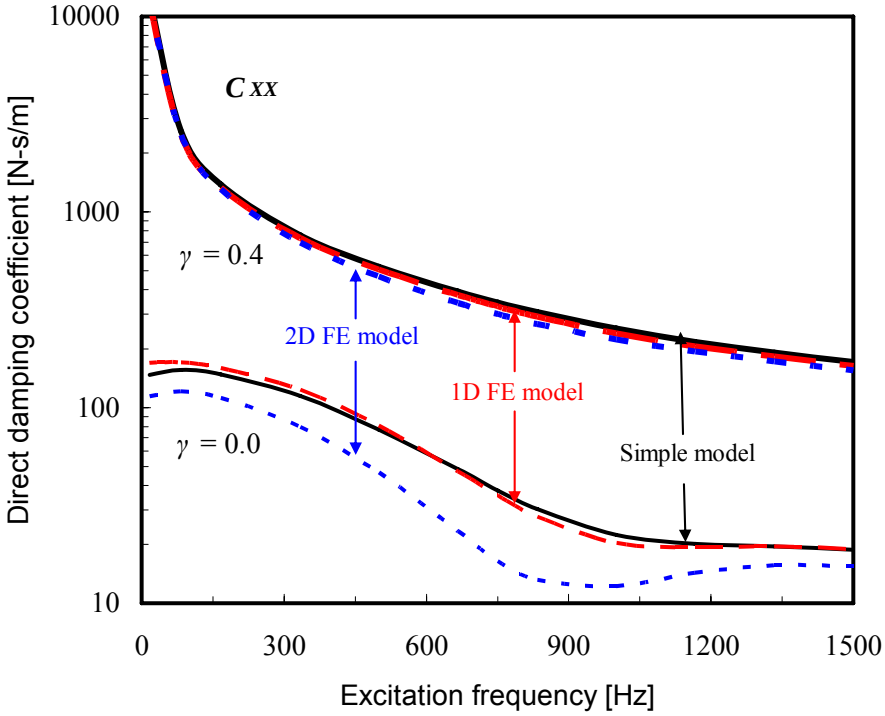
10000
1000
100
10
Direct damping coefficient [N-s/m]
C XX
γ = 0.4
γ = 0.0
2D FE model
1D FE model
Simple model
0
300
600
900
1200
1500
Excitation frequency [Hz]

(a) C_{XX}

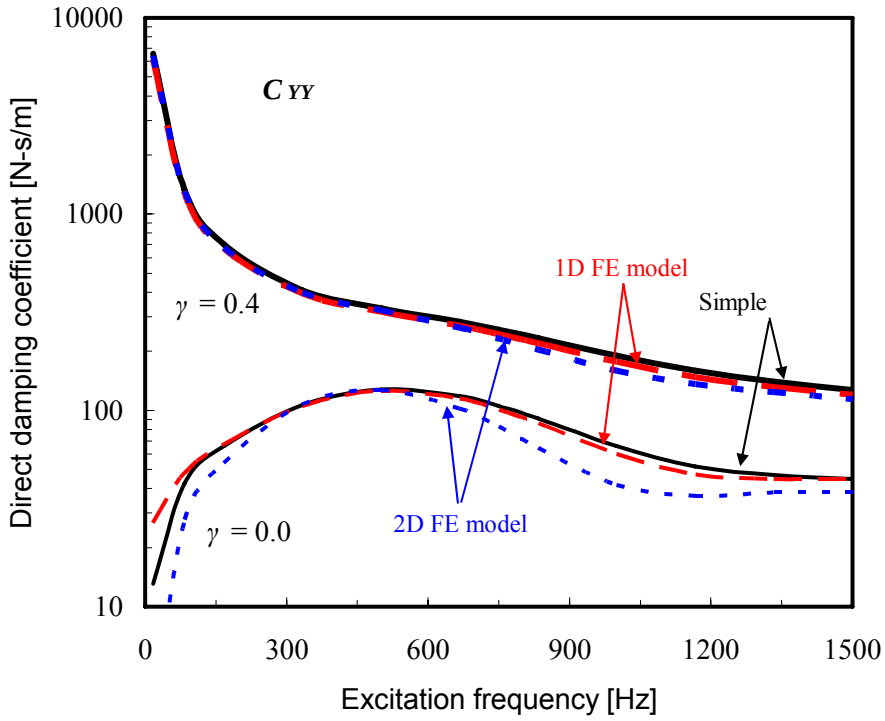
10000
1000
100
10
Direct damping coefficient [N-s/m]
C YY
γ = 0.4
γ = 0.0
1D FE model
Simple
2D FE model
0
300
600
900
1200
1500
Excitation frequency [Hz]

(b) C_{YY}

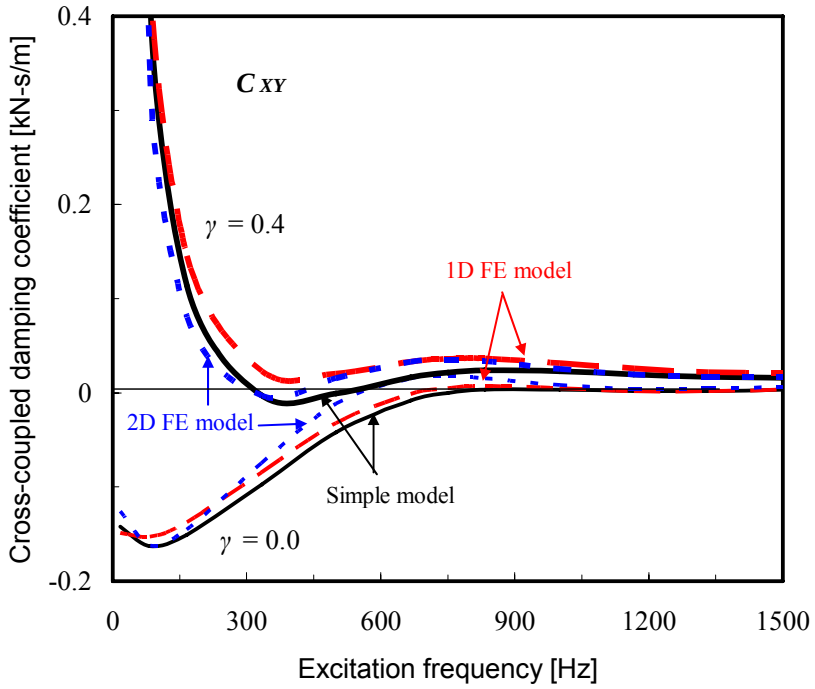

(c) C_{XY}

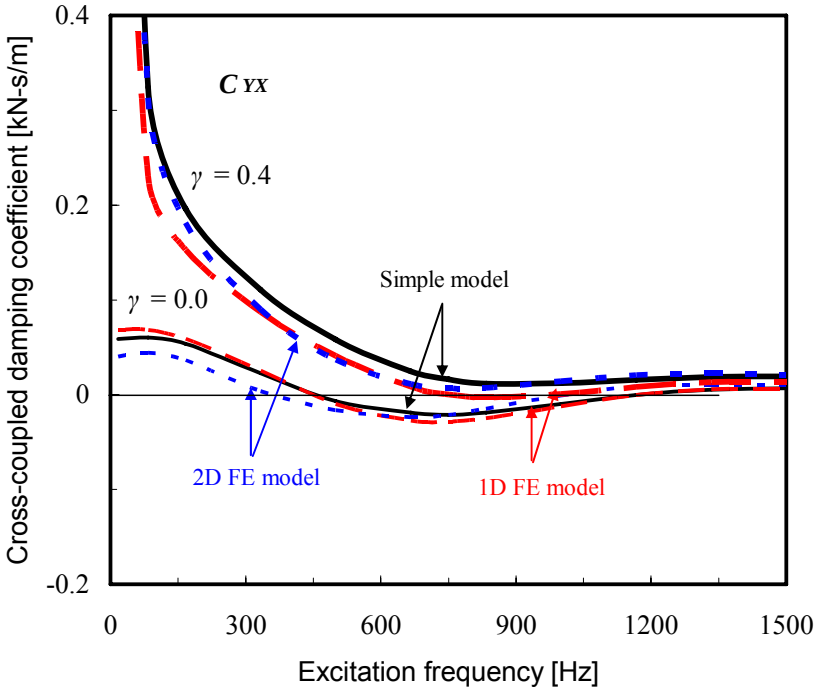

(d) C_{YX}

Figure 16. Predicted GFB damping coefficients versus excitation frequency for three structural models. Rotor speed: 45 krpm, Static load: 150 N. Structural loss factors, γ = 0.0 and 0.4

VI. COMPUTATIONAL TIME

In the present study, all analyses were conducted in a personal computer, Pentium® 4 processor (2.40 GHz CPU). The 1D structural model analysis requires much less computational time than the 2D model, due to a reduction in the degrees of freedom. While the 2D top foil model has 2,547 degrees of freedom, the 1D FE model has only 156. Therefore, in a particular case, the time to complete the 2D model analysis is ~10 seconds, while the 1D structural model analysis takes less than 1 second.

The perturbation analysis for calculation of force coefficients and implementing the FE stiffness matrices increases the computational cost as compared to the performance of the simple elastic foundation model analysis. For example, to find the static journal eccentricity and the synchronous force coefficients for an applied load of 50 N at 45,000 rpm, the 1D and 2D FE structural models need ~14 seconds and ~180 seconds, respectively, while the simpler model takes 9 seconds. Thus, the introduction of the 1D and 2D top foil structural models into the GFB predictive computational code increases the computational cost by 50% and 2000%, respectively. Note that the increase in computational time depends mainly on the number of degrees of freedom in the FE structure models.

VII. EFFECT OF MECHANICAL PRELOAD ON THE FORCED PERFORMANCE OF A GFB

Machined preloads in fluid film journal bearings aim to enhance the hydrodynamic wedge to generate a pressure field that produces a centering stiffness even in the absence of an applied static load [29]. The easiest way to introduce a preload into a GFB is by inserting metal shims underneath a bump strip and in contact with the bearing housing [30], as shown in Figure 17(a). The bump strip layers can also be manufactured with varying bump heights to introduce a preload more akin to those in a multiple lobe rigid surface bearing, see Figure 17(b). This second procedure is costly and probably inaccurate.

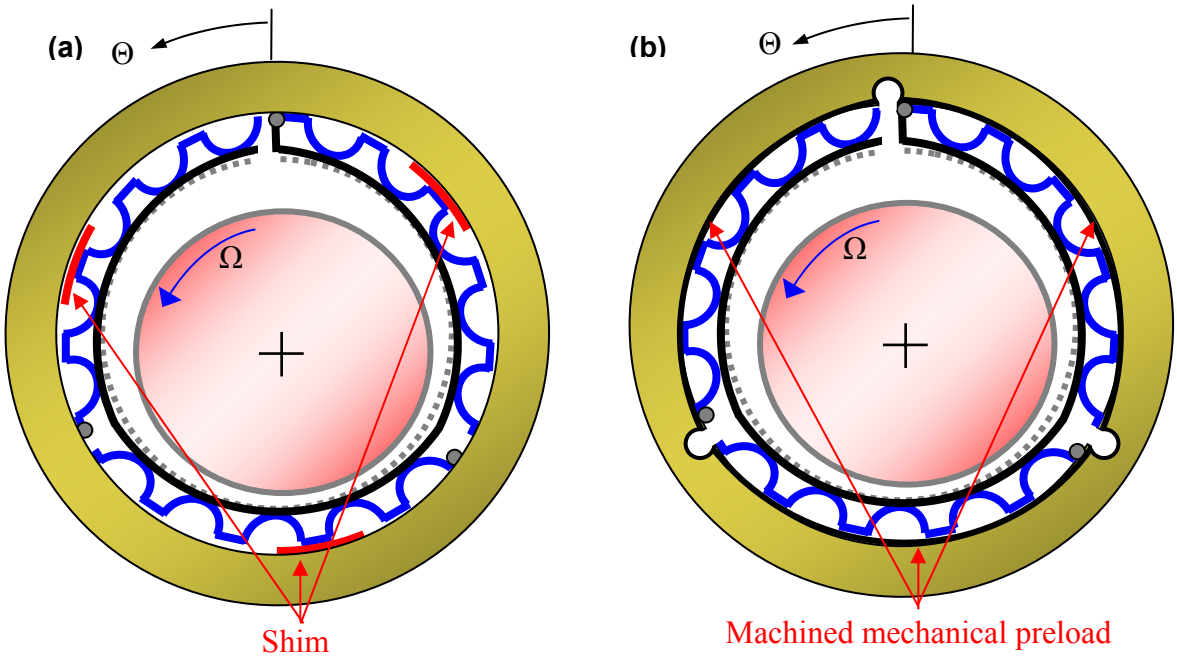

Figure 17. Schematic views of gas foil bearing with (a) shims and (b) with machined preloads

For analysis purposes, a GFB is construed as a "three lobe" configuration. Table 2 presents the material and dimensional characteristics of the bearing studied. The nominal clearance of the GFB equals 32 μm. Three shims of thickness 16 μm (~ 0.5 ×c) are inserted at the circumferential locations 60º, 180º, and 360º. Hence, the mechanically modified GFB has a dimensionless preload and offset ratio equal to 0.50 and 0.5, respectively. Design details for the top foil and the bump layer in GFBs are identical to those presented in Table 1. Predictions, derived from the uniform elastic foundation

model and from the 1D top foil model, show differences in performance characteristics for a GFB with and without the mechanical preload, i.e. simple GFB.

Table 2 Geometry of foil bearing with mechanical preload (shims)

Bearing radius, $R=D/2$	19.05 mm (0.75 inch)
Bearing length, L	38.1 mm (1.5 inch)
Top foil arc circumferential length, l_x	120 mm (4.7 inch)
Radial journal travel, c_J (~ clearance)	31.8 μm (1.25 mil)
Lobe arc angle	120 º
Shim arc angle*	40 º
Preload ratio**, r_p/c_J	0.5
Preload offset ratio	0.5
Shim thickness, t_s	16 μm (0.63 mil)
Number of shims, N_s	3
Shim material	Inconel X-750

* ~13 mm length in the circumferential direction.

** The clearance (c) for a GFB with preload uses the shim thickness. The nominal gap between the top foil and shaft follows the simple relationship $c(\theta)=\frac{3}{4}c_J+\frac{r_P}{2}\cos(3\theta)$ for θ E {0, 2π}.

Figure 18 displays, for increasing static loads, the predicted mid-plane pressure, structural deflection, and film thickness versus angular location. The film thickness is zoomed in between 90 º and 270 º. For a small static load of 5 N (specific load of 3.4 kPa or 0.5 psi), the GFB with preloads ensures hydrodynamic pressure generation and even deflects the foil structure, while the simple GFB does not, due to its mainly uniform film thickness ($h \sim c$) along the circumferential direction. As the static load increases, both the pressures and the structural deflections increase, and the minimum film thickness decreases. With increasing static loads, the preload effect in the GFB with shims vanishes due to the compliance of the bump strip layer. At high loads, the mechanical preload has little effect on the structural deflection, pressure and film thickness. The GFB whether it integrates shims (preload) or not shows identical performance for static loads exceeding the journal nominal clearance, as shown in Figures 19-22 for journal eccentricity and attitude angle, minimum film thickness and power loss.

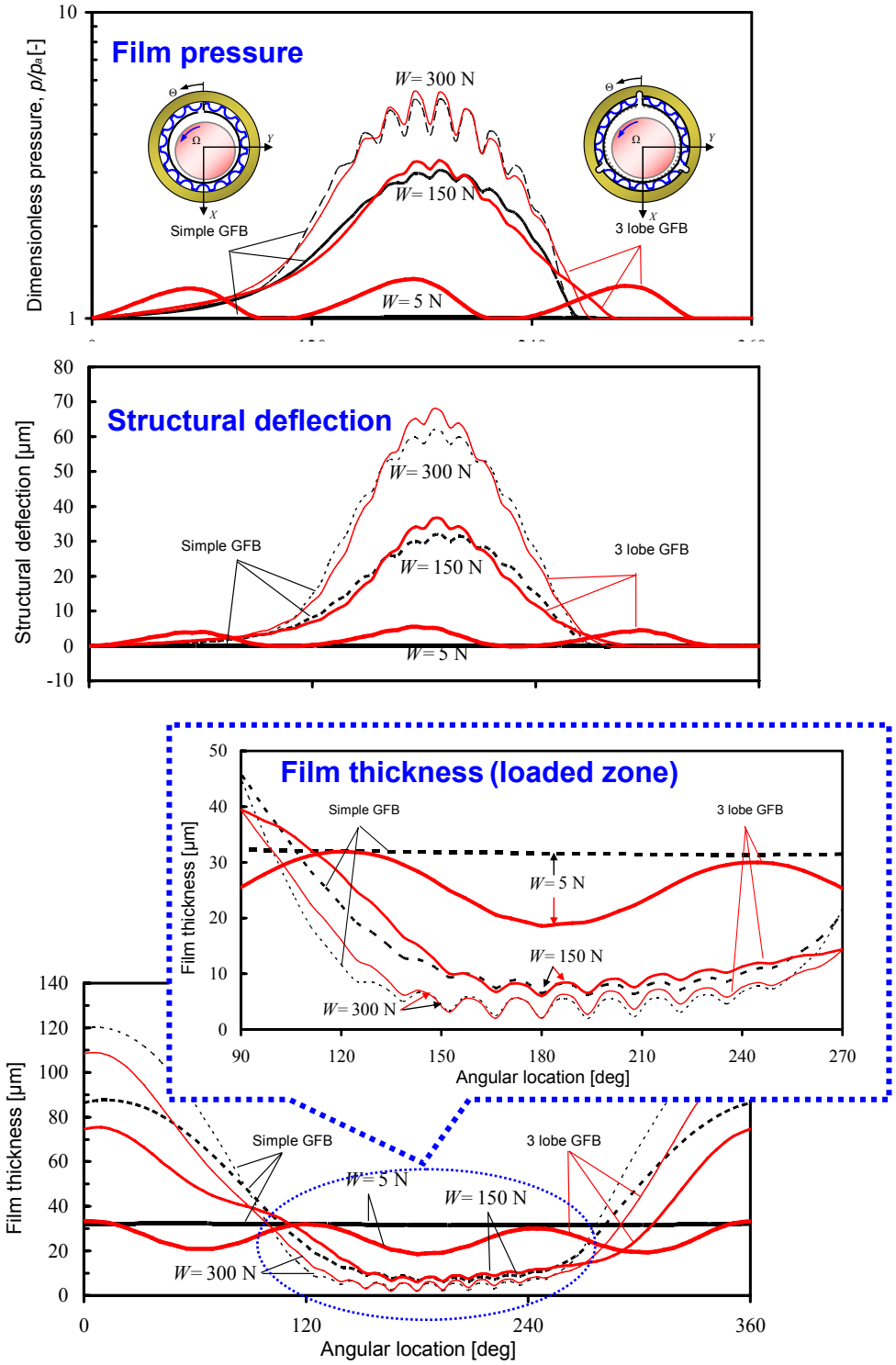

Figure 18. Dimensionless mid-plane pressure, structural deflection, and film thickness versus angular location for GFB with and without mechanical preload. Rotor speed: 45 krpm

Figure 19 depicts the GFB journal eccentricity versus static load applied along the *X* direction. With a mechanical preload, the GFB shows a linear relationship between load and journal position, i.e. a constant and uniform stiffness, since the gas film is stiffer even at low loads. The opposite behavior is evident for the GFB without shims, i.e. the journal eccentricity is not proportional to the applied load due to the softness of the gas film. For large loads, a linear behavior is notorious for journal eccentricities exceeding the bearing nominal clearance, c = 31.8 μm. The GFB with mechanical preload leads to consistently smaller journal static displacements than the simple GFB. From Figure 19, the difference between eccentricities is approximately equal to the mechanical preload, 16 μm; in particular at large loads.

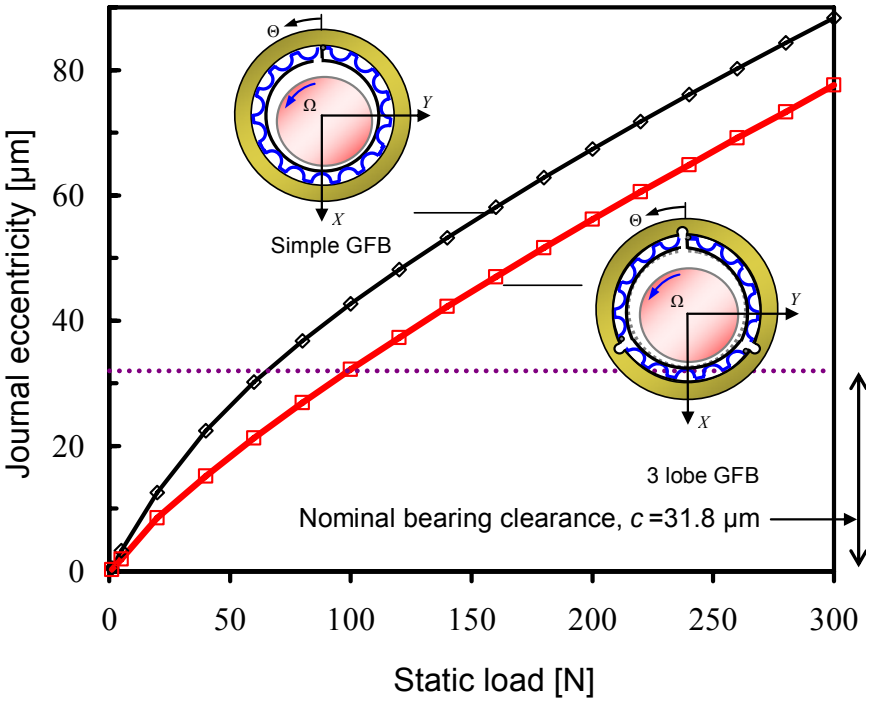

Figure 19. Journal eccentricity versus static load for GFB with and without mechanical preload. Rotor speed: 45,000 rpm

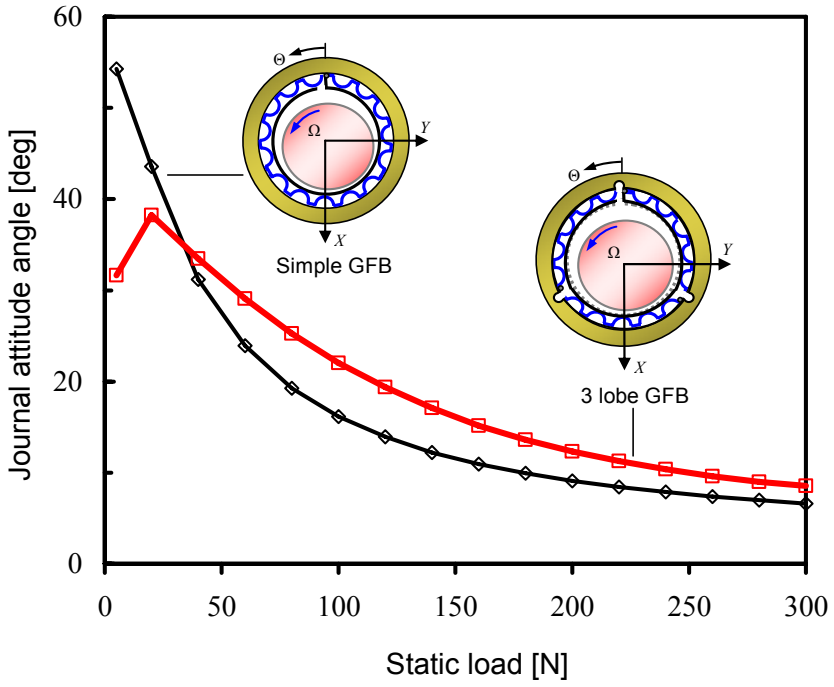

Figure 20. Journal attitude angle versus static load for for GFB with and without mechanical preload. Rotor speed: 45,000 rpm

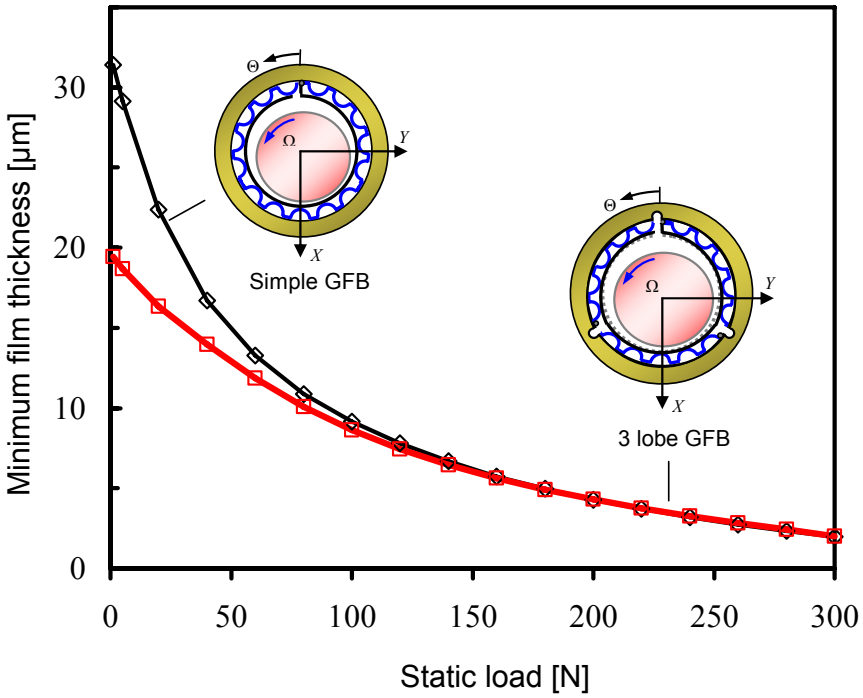

Figure 21. Minimum film thickness versus static load for GFB with and without mechanical preload. Rotor speed: 45,000 rpm

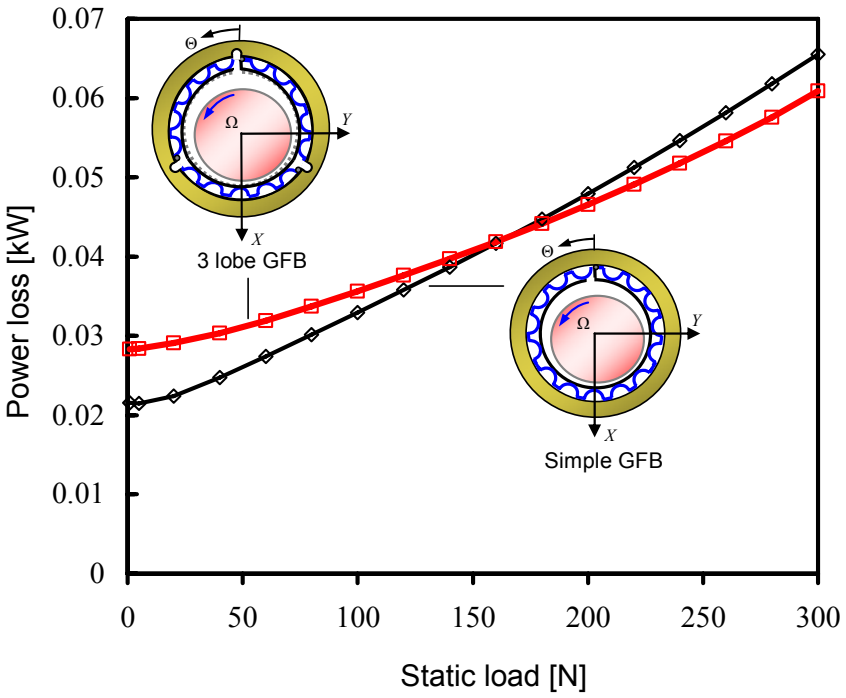

Figure 22. Drag power loss versus static load for GFB with and without mechanical preload. Rotor speed: 45,000 rpm

Figure 23 shows, for operation at 45 krpm, the synchronous stiffness and damping coefficients versus static load for the studied GFB, with and without a preload (shims). The predictions correspond to a structural loss factor $\gamma = 0.2$. In figures 23(a), the thick solid line with squares represents the bearing structural stiffness coefficient, K_{struc}. The GFB with preload, as expected, has larger direct stiffness coefficients, K_{XX} and K_{YY}, than the simple GFB, in particular at low static loads. The cross-coupled stiffness coefficients, K_{XY} and K_{YX}, for both bearing configurations are comparable in magnitude.

For the GFB with preload the direct damping coefficients, C_{XX} and C_{YY} shown in Figure 23(b), increase dramatically for low static loads. The damping increases effect is more pronounced for C_{XX} than for C_{YY}, and due to the reduced local clearance because of the shims. The magnitudes of cross-coupled damping coefficients, C_{XY} and C_{YX}, increase slightly for small static loads. In brief, the GFB with mechanical preload shows a significant increase in direct synchronous stiffness and damping coefficients for low static loads. This obvious advantage becomes less noticeable for large static loads.

Figure 24 displays the stiffness and damping coefficients versus excitation frequency. The operating speed is 45 krpm and small static load, just 5 N, applied along the X direction. As the excitation frequency increases, the direct stiffness coefficients, K_{XX} and K_{YY}, increase due to the hardening of the hydrodynamic gas film. Most importantly, while the cross-coupled stiffness $K_{XY} > K_{XX}$ and K_{YY} at low frequencies in the simple GFB; K_{XX} increases for the bearing with preload and is larger than the cross coupled stiffness. Direct damping coefficients, C_{XX} and C_{YY}, for the bearing with preload are larger at low frequencies than those of the simple GFB. The differences become minimal as the excitation frequency increases.

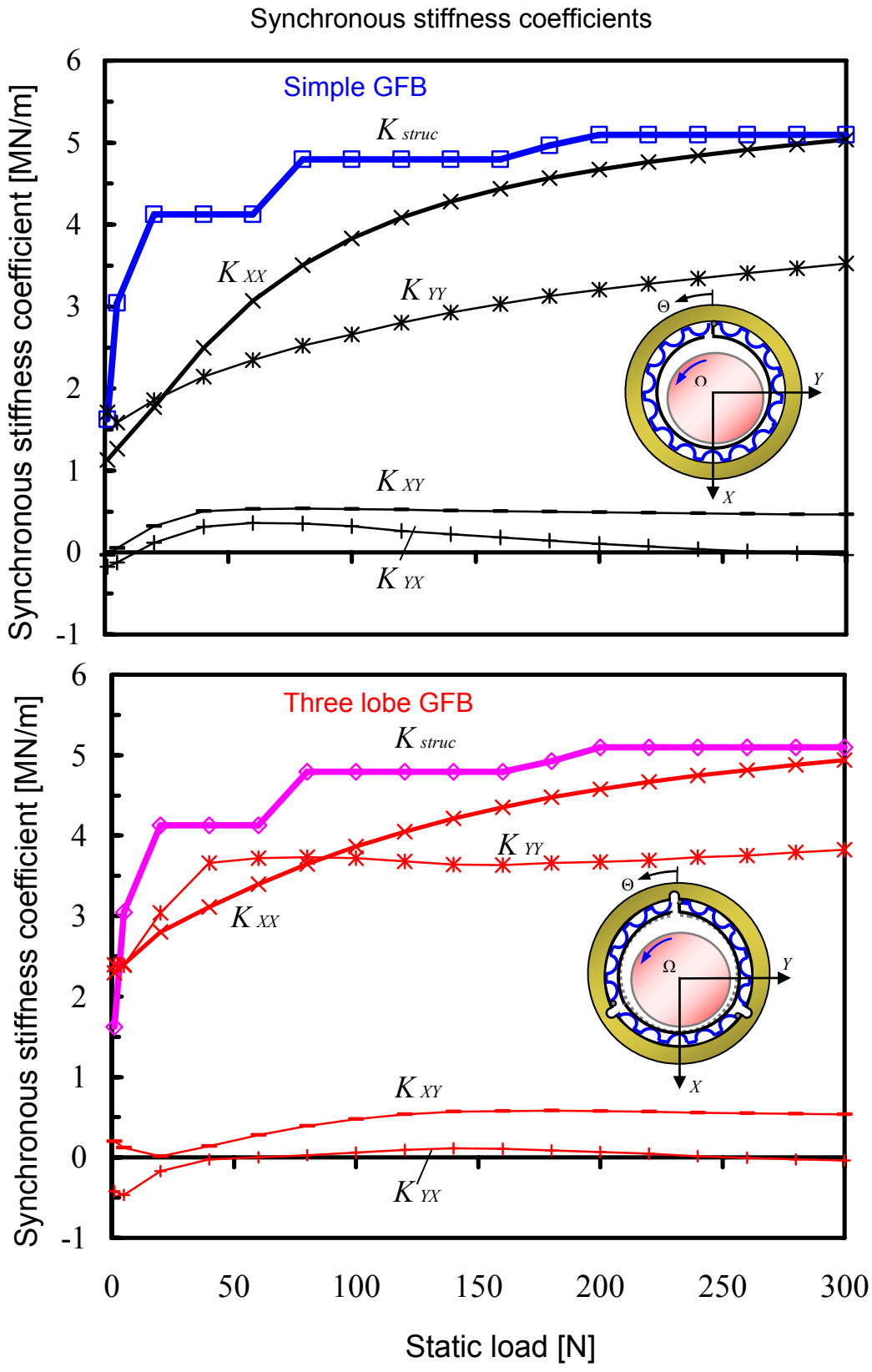

Figure 23a. Synchronous stiffness coefficients versus static load for GFB with and without preload. Rotor speed: 45,000 rpm, loss factor, γ=0.2

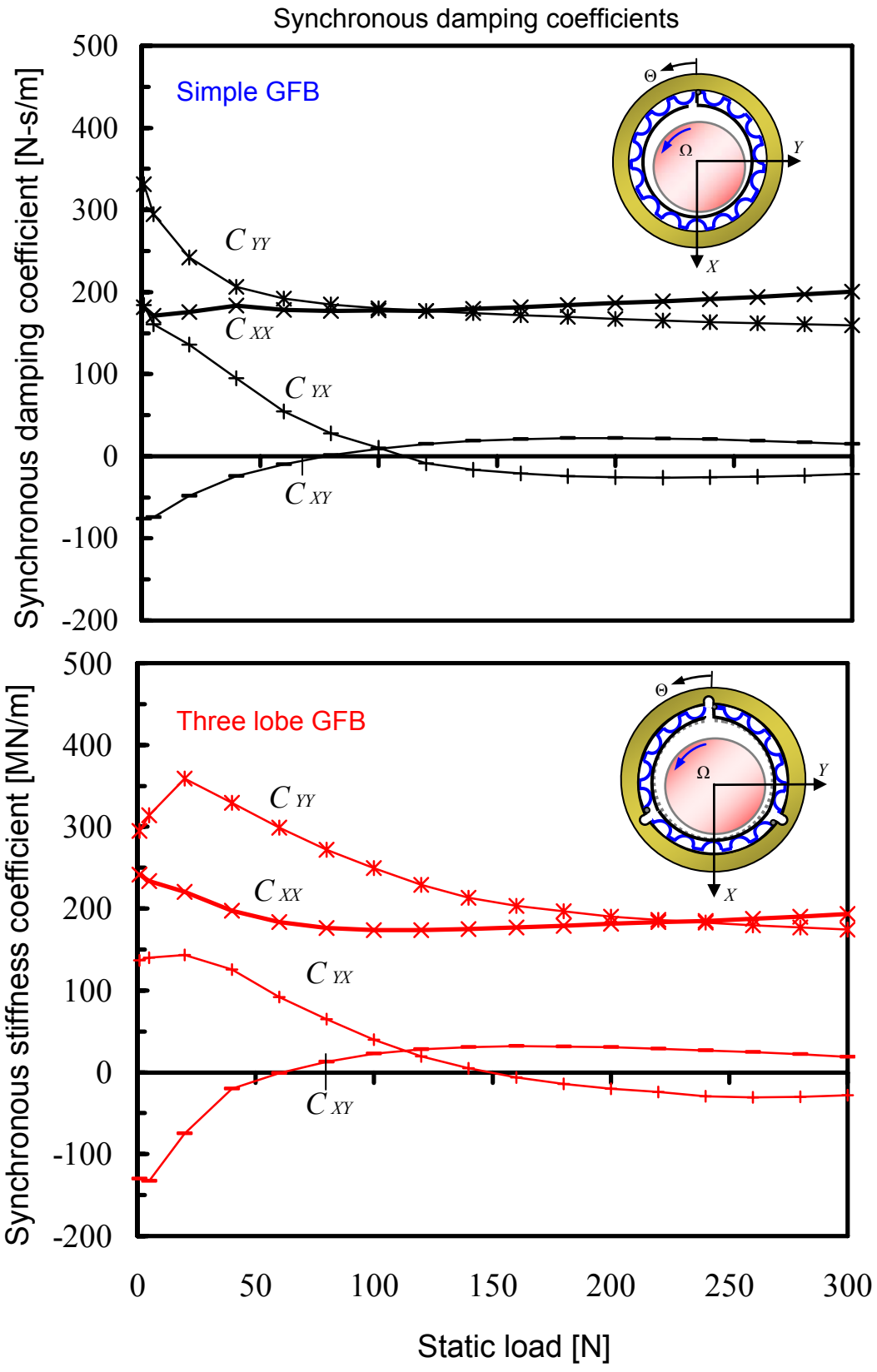

Figure 23b. Synchronous damping coefficients versus static load for GFB with and without preload. Rotor speed: 45,000 rpm, loss factor, γ=0.2

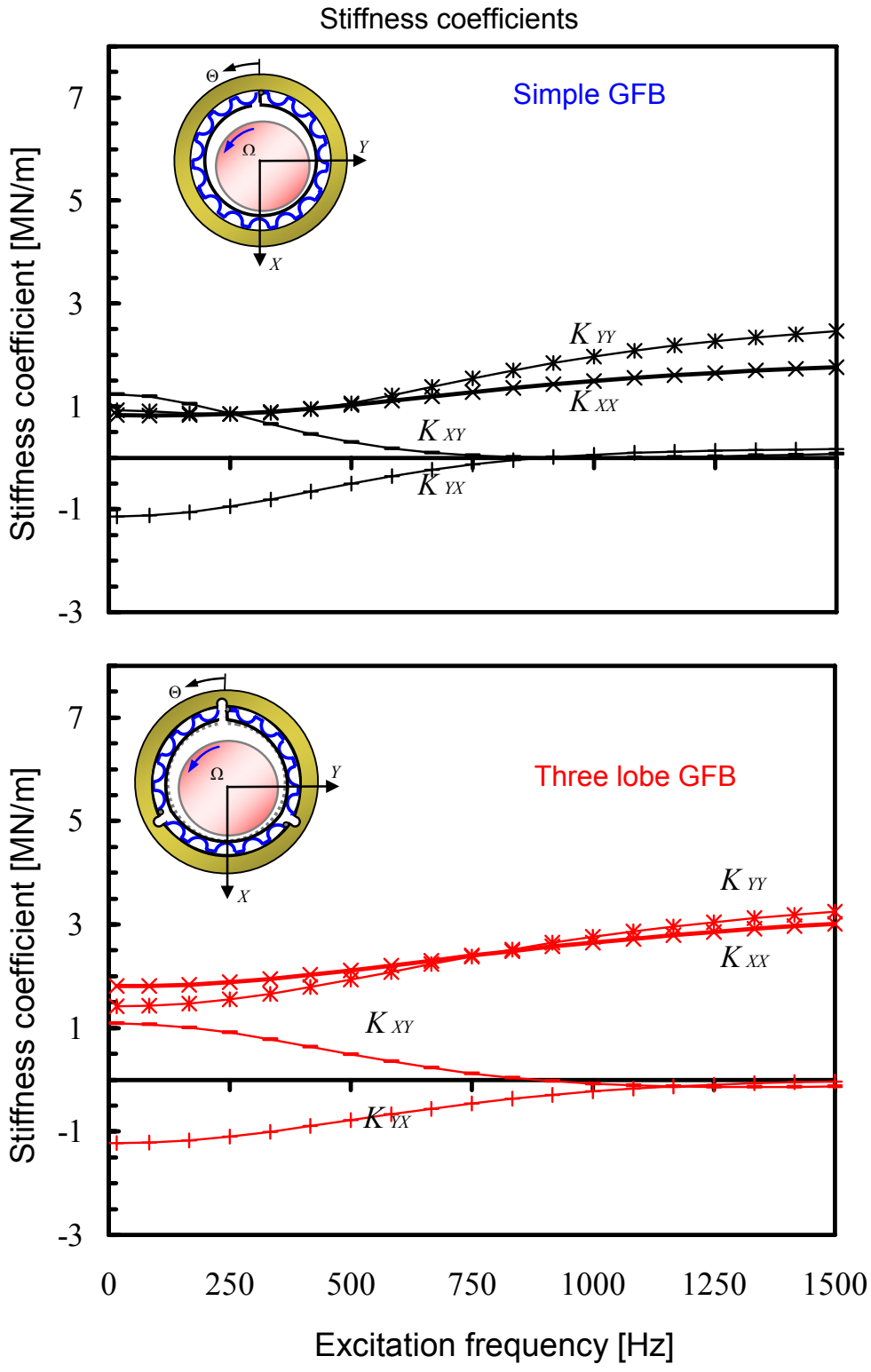

Figure 24(a) Stiffness coefficients versus excitation frequency for GFB with and without mechanical preload. Static load: 5N, rotor speed: 45 krpm, loss factor, γ=0.2

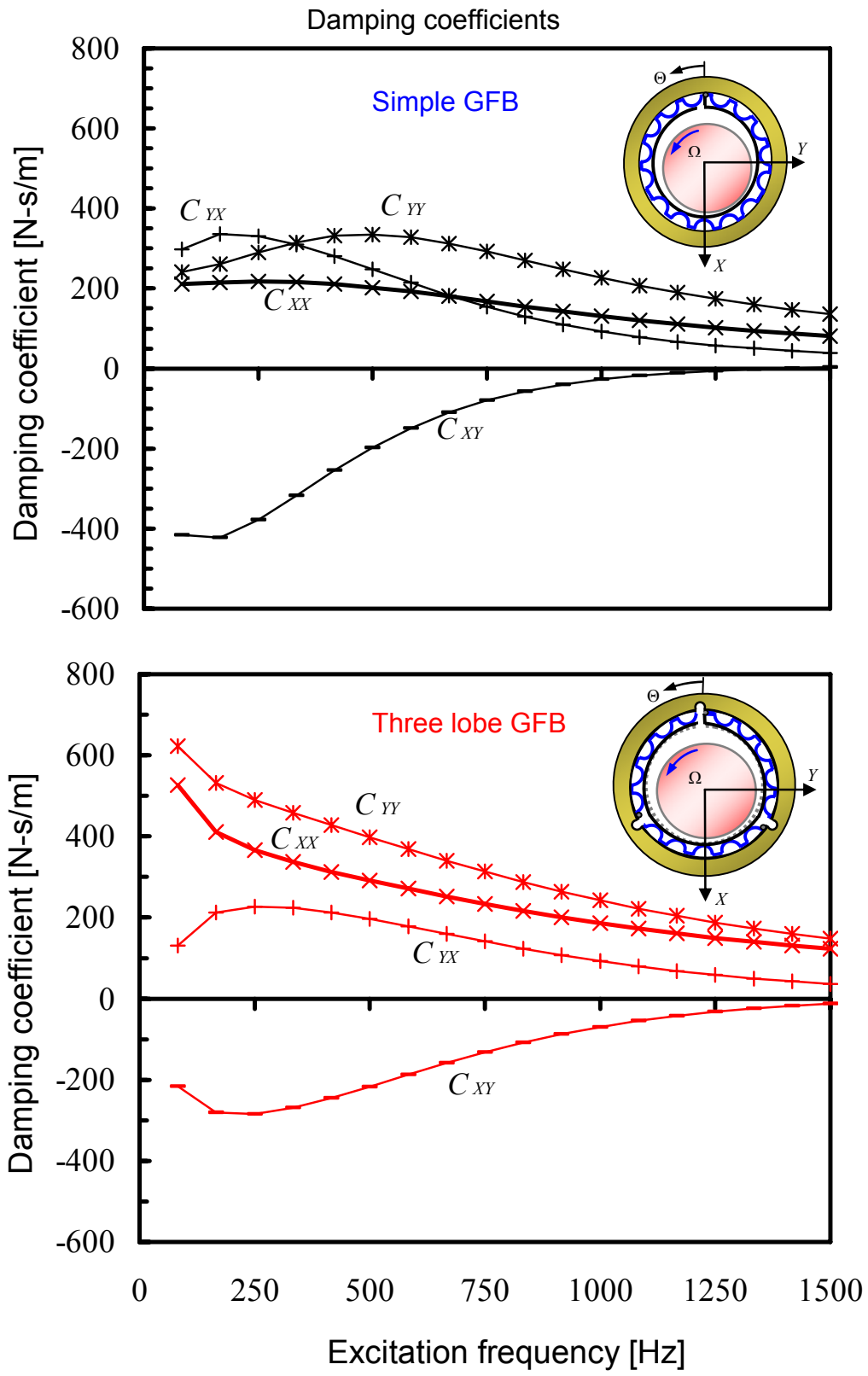

Figure 24(b) Damping coefficients versus excitation frequency for GFB with and without mechanical preload. Static load: 5N, rotor speed: 45 krpm, loss factor, γ=0.2

The energy imparted to the rotor (per period of motion) is,

$$E_{cycle} = \oint \left(F_X dX + F_Y dY \right) = \oint \left(F_X \dot{X} dt + F_Y \dot{Y} dt \right)$$

$$\text{where } \begin{Bmatrix} F_X \\ F_Y \end{Bmatrix} = -\begin{bmatrix} K_{XX} & K_{XY} \\ K_{YX} & K_{YY} \end{bmatrix} \begin{Bmatrix} X \\ Y \end{Bmatrix} - \begin{bmatrix} C_{XX} & C_{XY} \\ C_{YX} & C_{YY} \end{bmatrix} \begin{Bmatrix} \dot{X} \\ \dot{Y} \end{Bmatrix} \tag{8}$$

Consider rotor motions describing a forward whirl circular orbit, of amplitude A and frequency ω, i.e., $X = A\cos(\omega t)$ and $Y = A\sin(\omega t)$. Hence [31]:.

$$E_{cycle} = -Ar_{cycle} \left\{ \left(C_{XX} + C_{YY} \right) \omega - \left(K_{XY} - K_{YX} \right) \right\}$$

$$\text{where } Ar_{cycle} = \pi A^2 \tag{9}$$

The energy dissipated ($-E_{cycle}$) by the GFB uses the predictions of stiffness and damping coefficients for increasing frequencies and static loads. Figure 25 shows the predicted energy dissipated per unit area of circular orbit for a GFB with and without mechanical preload operating at 45,000 rpm (750 Hz). For low loads, 5N and 50 N, the GFB with and without shims are unstable (negative dissipated energy) and with identical threshold frequencies, namely 270 Hz and 350 Hz, respectively. The threshold frequency notes when the energy turns positive, thus actually dissipating energy to reduce vibrations. Regardless of preload, the GFB is stable for the largest load (150 N) over the entire frequency range. Although there is not a significant difference in the threshold frequency ($\omega_{\text{threshold}}$), the threshold speed of instability ($\Omega_{threshold}$) will increase when including a mechanical preload (shim) because the bearing direct stiffness will increase the system natural frequency (ω_n) of the rigid rotor-GFB system, i.e., $\Omega_{threshold} = \omega_n/WFR$. This observation is strictly applicable to a rigid rotor-bearing system.

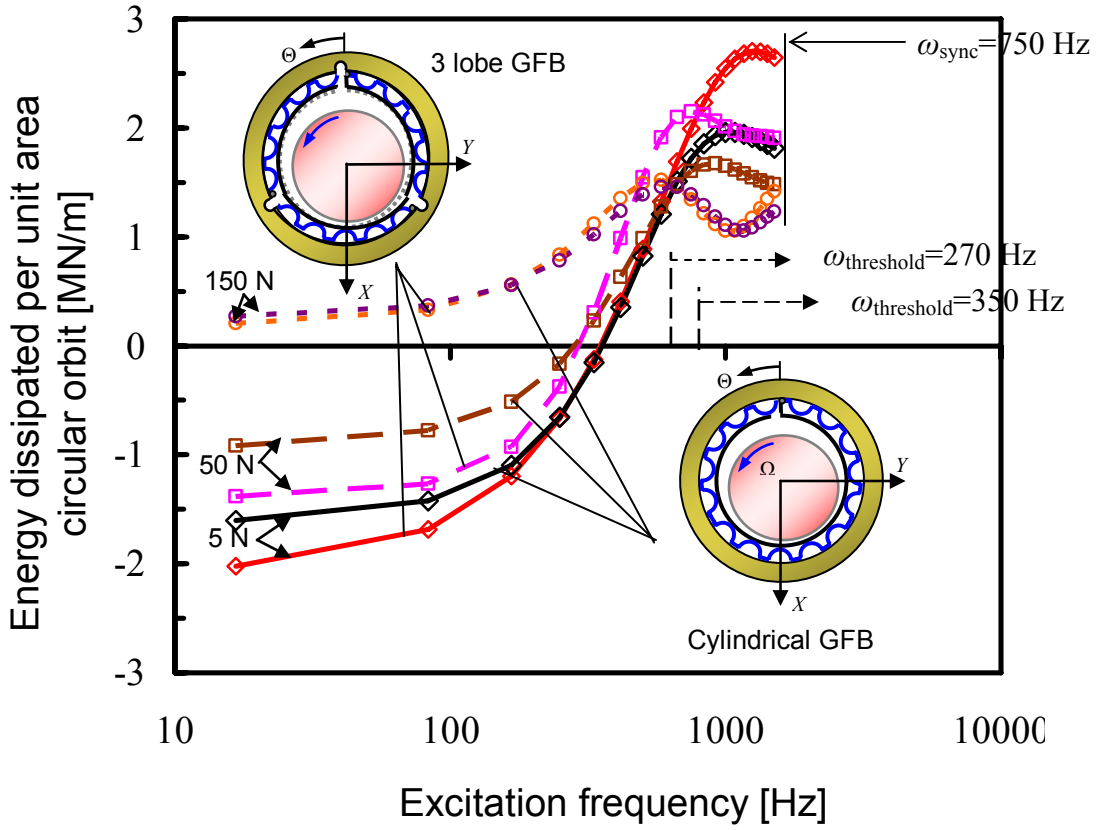

Figure 25. Energy dissipated by a GFB with and without mechanical preload for increasing static loads. Rotor speed: 45 krpm (750 Hz), loss factor, γ=0.2

VIII. CLOSURE

Conventional analyses of GFBs neglect the elasticity of the top foil and consider the bump strip layers support structure as an elastic foundation with uniform stiffness. This simple model has been most useful for decades; however, stringent applications of gas bearings into commercial oil-free turbomachinery demands the development of more realistic models to better engineer them as reliable supports.

Presently, the report introduces two finite element models for the top foil elastic structure. The simplest FE model assumes the top foil as a 1D beam with negligible deflections along the axial coordinate, i.e. infinitely stiff and acted upon by a uniformly distributed pressure field. The second FE model, 2D, takes the top foil as a flat shell with anisotropic material properties. The underlying bumps modeled as a uniform elastic foundation along the edge of a typical finite element representing a top foil, are directly integrated into a global stiffness matrix that relates the top foil (and bumps) deflections to applied gas film pressure or contact pressure, depending on the operating condition. The decomposition of the symmetric stiffness matrix into upper and lower triangular parts is performed off-line and prior to computations coupling it to the gas bearing analysis. The procedure greatly enhances the computational efficiency of the numerical scheme.

Predictions of load capacity, attitude angle, and minimum film thickness versus journal speed are obtained for a gas foil bearing tested decades ago [19]. This reference is, to date, the only one with full details on bearing configuration and structural properties. The predictions presented correspond to three models: (a) simplest elastic foundation with no accounting for top foil structure, (b) 1D FE model with top foil as a thin beam, and (c) 2D FE model with top foil as a shell.

2D FE model predictions overestimate the minimum film thickness at the bearing centerline, but underestimate it at the bearing edges. Predictions from the 1D FE model compare best to the limited tests data; reproducing closely the experimental circumferential profile of minimum film thickness reported in [19]. The 1D top foil model is to be preferred due to its low computational cost. The FE models predictions show local *ripples* in the top foil supported in between bumps. The *ripples* are a pathway for gas to escape out of the bearing, thus decreasing the hydrodynamic pressure and diminishing the bearing load carrying capacity.

Predicted stiffness and damping coefficients versus excitation frequency show that the two FE top foil structural models result in slightly lower direct stiffness and damping coefficients than those from the simple elastic foundation model.

A three lobe GFB with mechanical preloads, introduced by inserting shims underneath the bump strips, is analyzed using the 1D FE structural model. Predictions show the mechanical preload enhances the load capacity of the gas foil bearing for operation at low loads and low shaft speeds. Energy dissipation, a measure of the bearing ability to ameliorate vibrations, is not affected by the preload induced although the direct stiffness of the bearings is of importance for operation at high speeds with low load conditions. Mechanical preload has no effect on the static and dynamic forced performance of GFBs supporting large static loads.

IX. REFERENCES

[1] Agrawal, G. L., 1997, "Foil Air/Gas Bearing Technology – an Overview," ASME Paper No. 97-GT-347.

[2] Heshmat, H., and Hermel, P., 1993, "Compliant Foil Bearings Technology and Their Application to High Speed Turbomachinery," Thin Films in Tribology, pp. 559-575.

[3] Barnett, M. A., and Silver, A., 1970, "Application of Air Bearing to High-Speed Turbomachinery," SAE Paper No. 700720.

[4] Emerson, T. P., 1978, "The Application of Foil Air Bearing Turbomachinery in Aircraft Environmental Control Systems," Paper No. 780-ENAS-18, *ASME Proc. Intersociety Conference on Environmental System*, San Diego, CA, July 10-13.

[5] Heshmat, C. A., Heshmat, H., 1995, "An Analysis of Gas-Lubricated, Multileaf Foil Journal Bearings with Backing Springs," J. Tribol., **117**, pp. 437-443.

[6] Braun, M. J., Choy, F. K., Dzodzo, M., and Hsu, J., 1996, "Two-Dimensional Dynamic Simulation of a Continuous Foil Bearing," Tribol. Intl., **29**(1), pp. 61-68.

[7] DellaCorte, C., and Valco, M. J., 2000, "Load Capacity Estimation of Foil Air Journal Bearings for Oil-Free Turbomachinery Applications," NASA/TM—2000-209782.

[8] Heshmat, H., 1994, "Advancements in the Performance of Aerodynamic Foil Journal Bearings: High Speed and Load Capacity," J. Tribol., **116**, pp. 287-295.

[9] Heshmat, H., Walowit, J. A., and Pinkus, O., 1983, "Analysis of Gas-Lubricated Foil Journal Bearings," J. Lubr. Tech., **105**, pp. 647-655.

[10] San Andrés, L., 1995, "Turbulent Flow Foil Bearings for Cryogenic Applications," J. Tribol., **117**, pp. 185-195.

[11] Blok, H. and vanRossum, J. J., 1953, "The Foil Bearing – A New Departure In hydrodynamic Lubrication," Lubr. Eng., December, pp 316-320.

[12] Heshmat, H., Walowit, J. A., and Pinkus, O., 1983, "Analysis of Gas Lubricated Compliant Thrust Bearings," J. Lubr. Tech., **105**, pp 638-646.

[13] Peng, J.-P., and Carpino, M., 1993, "Calculation of Stiffness and Damping Coefficients for Elastically Supported Gas Foil Bearings," J. Tribol., **115**, pp 20-27.

[14] Peng, J.-P., and Carpino, M., 1994, "Coulomb Friction Damping Effects in Elastically Supported Gas Foil Bearings," STLE Tribol. Trans., **37**(1), pp 91-98.

[15] Carpino, M., Medvetz, L. A., and Peng, J.-P., 1994, "Effects of Membrane Stresses in the Prediction of Foil Bearing Performance," STLE Tribol. Trans., **37**, pp 43-50.

[16] Carpino, M., Peng, J.-P., and Medvetz, L. A., 1994, "Misalignment In A Complete Shell Gas Foil Journal Bearing," STLE Tribol. Trans., **37**, pp. 829-835.

[17] Carpino M., Talmage, G., 2003, "A Fully Coupled Finite Element Formulation for Elastically Supported Foil Journal Bearings," STLE Tribol. Trans., **46**, pp 560-565.

[18] Kim, T. H., and San Andrés, L., 2005, "Heavily Loaded Gas Foil Bearings: a Model Anchored to Test Data," ASME Paper No. GT2005-68486.

[19] Ruscitto, D., Mc Cormick, J., and Gray, S., 1978, "Hydrodynamic Air Lubricated Compliant Surface Bearing For An Automotive Gas Turbine Engine I-Journal Bearing Performance," NASA CR-135368.

[20] Ku, C.-P. and Heshmat, H., 1993, "Compliant Foil Bearing Structural Stiffness Analysis – Part II: Experimental Investigation," J. Tribol., **115,** July, pp 364-369.

[21] Lee, D.–H., Kim, Y.-C., Kim, K.-W., 2004, "The Static and Dynamic Performance Analyses of Air Foil Journal Bearings for Various Bump Foil Stiffness," J. KSTLE, **20**(5), pp. 245-251.

[22] Reddy, J. N., 1993, *An Introduction to the Finite Element Method*, McGRAW-HILL.

[23] Timoshenko, S. P., and Woinowsky-Krieger, S., 1959, *Theory of Plates and Shells*, McGRAW-HILL.

[24] Crandall, S. H., Dahl, N. C., and Lardner, T. J., 1972, *An Introduction to the Mechanics of Solids*, McGRAW-HILL.

[25] Iordanoff, I., 1999, "Analysis of an Aerodynamic Compliant Foil Thrust Bearing: Method for a Rapid Design," J. Tribol., **121**, pp. 816-822.

[26] Numerical Recipes in Fortran 77: The Art of Scientific Computing, ISBN 0-521-43064-X, Cambridge University Press, pp. 89-91.

[27] Faria, M., and San Andrés, L., 2000, "On the Numerical Modeling of High speed Hydrodynamic Gas Bearing," J. Tribol., **122**, pp. 124-130.

[28] Ertas, B. H., and Vance, J. M., 2005, "The Inflence of Same-Sign Cross-Coupled Stiffness on Rotordynamics," ASME Paper No. DETC2005-84873.

[29] San Andrés, L., 1996, "Turbulent Flow, Flexure-Pivot Hybrid Bearings for Cryogenic Applications," J. Tribol., **118**, pp. 190–200.

[30] Chen, H. M., Howarth, R., Theilacker, J. C., and Soyars, W. M., "Application of Foil Bearings to Helium Turbocompressor," *Proceedings of the 30th Turbomachinery Symposium*, Turbomachinery Laboratory, Texas A&M University, pp. 103-113.

[31] Adams, M. L., 2001, *Rotating Machinery Vibration – from analysis to troubleshooting*, Marcel Dekker, New York, pp. 62-70.

APPENDIX A. 1D FINITE ELEMENT FORMULATION FOR TOP FOIL

The weak form of Eq. (4) over a finite element domain becomes [22]:

$$0=\int_{x_e}^{x_{e+1}}\left(EI\frac{d^2v_1}{d^2x}\frac{d^2w}{d^2x}-v_1q\cdot L\right)dx-v_1(x_e)Q_1^e-\left(-\frac{dv_1}{dx}\right)\Big|_{x_e}Q_2^e-v_1(x_{e+1})Q_3^e-\left(-\frac{dv_1}{dx}\right)\Big|_{x_e+1}Q_4^e \quad \text{(A-1)}$$

where $v_1(x)$ and L are weight function and top foil width, respectively. Q_1^e and Q_3^e denote the shear forces, and Q_2^e and Q_4^e denote the bending moments at the boundary of an element, i.e.,

$$\begin{aligned} Q_1^e &\equiv \left[\frac{d}{dx}\left(EI\frac{d^2w}{dx^2}\right)\right]\Big|_{x_e}; \qquad Q_2^e \equiv \left(EI\frac{d^2w}{dx^2}\right)\Big|_{x_e}; \\ Q_3^e &\equiv -\left[\frac{d}{dx}\left(EI\frac{d^2w}{dx^2}\right)\right]\Big|_{x_e+1}; \quad Q_4^e \equiv -\left(EI\frac{d^2w}{dx^2}\right)\Big|_{x_e+1} \end{aligned} \quad \text{(A-2)}$$

An appropriate interpolation function w must satisfy the essential boundary conditions, i.e.

$$w^e=\sum_{j=1}^{4}u^e{}_j\psi_j^e=u^e{}_1\psi_1^e+u^e{}_2\psi_2^e+u^e{}_3\psi_3^e+u^e{}_4\psi_4^e \quad \text{(A-3)}$$

transverse deflection (w_1, w_2) angle (θ_1, θ_2)

where $\left\{\psi^e\right\}_j^4$ is the set of Hermite cubic interpolation function [22].

Setting $v=\left\{\psi^e\right\}_j^4$ and substitution of Eq. (A-3) into Eqn (A-1) yields the force equation

$$\left[K^e\right]\left\{U^e\right\}=\left\{F^e\right\} \quad \text{(A-4)}$$

where

$$\left[K^e\right]=\frac{2b}{l_{ex}^3}\begin{bmatrix}6 & -3l_{ex} & -6 & -3l_{ex}\\ -3l_{ex} & 2l_{ex}^2 & 3l_{ex} & l_{ex}^2\\ -6 & 3l_{ex} & 6 & 3l_{ex}\\ -3l_{ex} & l_{ex}^2 & 3l_{ex} & 2l_{ex}{}^2\end{bmatrix},\quad \left\{U^e\right\}=\begin{Bmatrix}u_1^e\\ u_2^e\\ u_3^e\\ u_4^e\end{Bmatrix} \text{ and } \left\{F^e\right\}=\frac{q\cdot L\cdot l_{ex}}{12}\begin{Bmatrix}6\\ -l_{ex}\\ 6\\ l_{ex}\end{Bmatrix}+\begin{Bmatrix}Q_1\\ Q_2\\ Q_3\\ Q_4\end{Bmatrix} \qquad \text{(A-5)}$$

with l_{ex} is a FE (top foil) length. Above $[K^e]$ is the element stiffness matrix and $\{F^e\}$ is the nodal force vector.

The bump stiffness matrix $[K^s]$ is added at the appropriate locations when assembling the global stiffness matrix $[K^G]$.

$$\left[K^s\right]=K_l\begin{bmatrix}1 & 0 & 0 & 0\\ 0 & 0 & 0 & 0\\ 0 & 0 & 1 & 0\\ 0 & 0 & 0 & 0\end{bmatrix} \quad \text{where } K_l=K_f\times L\times s_0 \qquad \text{(A-6)}$$

K_f, and s_0 are the bump structural stiffness per unit area, and bump pitch, respectively. Note that when considering the dynamic behavior of bump supports, a complex stiffness $K_f{}'=K_f\left(1+i\gamma\right)$ includes a bump structural loss factor (γ) arising from material hysteresis and dry-friction.

APPENDIX B. 2D FINITE ELEMENT FORMULATION FOR TOP FOIL

Substituting Eq. (6) into Eq. (5) leads to

$$\frac{\partial}{\partial x}\left[A_{55}\left(\phi_x+\frac{\partial w}{\partial x}\right)\right]+\frac{\partial}{\partial y}\left[A_{44}\left(\phi_y+\frac{\partial w}{\partial y}\right)\right]=q\ ;$$

$$\frac{\partial}{\partial x}\left[D_{11}\frac{\partial \phi_x}{\partial x}+D_{12}\frac{\partial \phi_y}{\partial x}\right]+\frac{\partial}{\partial y}\left[D_{66}\left(\frac{\partial \phi_x}{\partial y}+\frac{\partial \phi_y}{\partial x}\right)\right]-A_{55}\left(\phi_x+\frac{\partial w}{\partial x}\right)=0\ ; \tag{B-1}$$

$$\frac{\partial}{\partial x}\left[D_{66}\left(\frac{\partial \phi_x}{\partial y}+\frac{\partial \phi_y}{\partial x}\right)\right]+\frac{\partial}{\partial y}\left[D_{12}\frac{\partial \phi_x}{\partial x}+D_{22}\frac{\partial \phi_y}{\partial y}\right]-A_{44}\left(\phi_y+\frac{\partial w}{\partial y}\right)=0$$

Over a FE, the weak form of Eq. (B-1) is

$$0=\int_{\Omega_e}\left\{\frac{\partial v_1}{\partial x}\left[A_{55}\left(\phi_x+\frac{\partial w}{\partial x}\right)\right]+\frac{\partial v_1}{\partial y}\left[A_{44}\left(\phi_y+\frac{\partial w}{\partial y}\right)\right]-v_1 q\right\}dxdy-\oint_{\Gamma_e} v_1\left[Q_n\right]dx\ ;$$

$$0=\int_{\Omega_e}\left\{\frac{\partial v_2}{\partial x}\left[D_{11}\frac{\partial \phi_x}{\partial x}+D_{12}\frac{\partial \phi_y}{\partial x}\right]+\frac{\partial v_2}{\partial y}\left[D_{66}\left(\frac{\partial \phi_x}{\partial y}+\frac{\partial \phi_y}{\partial x}\right)\right]-v_2 A_{55}\left(\phi_x+\frac{\partial w}{\partial x}\right)\right\}dxdy\ ;$$
$$-\oint_{\Gamma_e} v_2\left[M_n\right]dx \tag{B-2}$$

$$0=\int_{\Omega_e}\left\{\frac{\partial v_3}{\partial x}\left[D_{66}\left(\frac{\partial \phi_x}{\partial y}+\frac{\partial \phi_y}{\partial x}\right)\right]+\frac{\partial v_3}{\partial y}\left[D_{12}\frac{\partial \phi_x}{\partial x}+D_{22}\frac{\partial \phi_y}{\partial y}\right]-v_3 A_{44}\left(\phi_y+\frac{\partial w}{\partial y}\right)\right\}dxdy$$
$$-\oint_{\Gamma_e} v_3\left[M_{ns}\right]ds$$

where $v_{i,\ i=1\text{-}3}$ is a weight function. At the element boundary, M_n and M_{ns} are bending moments, and Q_n is the shear force. Within the domain of a FE, w, ϕ_x and ϕ_y are of the form

$$w=\sum_{j=1}^{n} w_j\psi_j^1\ ,\ \phi_x=\sum_{j=1}^{m}\phi_{x_j}\psi_j^2\ ,\ \phi_y=\sum_{j=1}^{m}\phi_{y_j}\psi_j^2\ \text{ where }\ \psi_j^1=\psi_j^2=\psi_j \tag{B-3}$$

and using Lagrange's bilinear interpolation functions yields the element stiffness matrix $[K^e]$ and force vector $\{F^e\}$ for a linear rectangular element. Note that $n = m = 4$ in Eq. (B-3) for 4-node finite elements. The finite element structural equation for the shell element is:

$$[K^e]\ \{U^e\} = \{F^e\} \tag{B-4}$$

where

$$[K^e] = \begin{bmatrix} [k^{11}] & [k^{12}] & [k^{13}] \\ & [k^{22}] & [k^{23}] \\ \text{Symmetric} & & [k^{33}] \end{bmatrix};\ \{U^e\} = \begin{Bmatrix} \{w\} \\ \{\phi_x\} \\ \{\phi_y\} \end{Bmatrix};\ \{F^e\} = \begin{Bmatrix} \{f^1\} \\ \{m^1\} \\ \{m^2\} \end{Bmatrix} \tag{B-5}$$

$[k^{ij}]_{4\times4}$ depicts direct and cross-coupled (symmetric) stiffness matrices for a four-node finite element. $\{w\}_{4\times1}$ represents the transverse deflection vector, and $\{\phi_x\}_{4\times1}$ and $\{\phi_y\}_{4\times1}$ are rotations of the transverse normal about the *y* and *x* axes, respectively, for four-node linear rectangular elements. $\{f^l\}_{4\times1}$ is the normal load vector, and $\{m^1\}_{4\times1}$ and $\{m^2\}_{4\times1}$ are bending moment vectors for the *x* and *y* axes, respectively. $[K^e]_{12\times12}$, $\{U^e\}_{12\times1}$, and $\{F^e\}_{12\times1}$ make up the element stiffness matrix, deflection vector, and force vector, respectively. The components of the sub-matrices, $k^{ij}{}_{i,j\,=\,1\text{-}3}$ is given in [22].

$$\begin{aligned}
k_{ij}^{11} &= \int_{\Omega_e}\left(A_{55}\frac{\partial\psi_i}{\partial x}\frac{\partial\psi_j}{\partial x} + A_{44}\frac{\partial\psi_j}{\partial y}\frac{\partial\psi_j}{\partial y}\right)dxdy \\
k_{ij}^{12} &= \int_{\Omega_e}\left(A_{55}\frac{\partial\psi_i}{\partial x}\psi_j\right)dxdy \\
k_{ij}^{13} &= \int_{\Omega_e}\left(A_{44}\frac{\partial\psi_i}{\partial x}\psi_j\right)dxdy \\
k_{ij}^{22} &= \int_{\Omega_e}\left(D_{11}\frac{\partial\psi_i}{\partial x}\frac{\partial\psi_j}{\partial x} + D_{66}\frac{\partial\psi_i}{\partial y}\frac{\partial\psi_j}{\partial y} + A_{55}\psi_i\psi_j\right)dxdy \\
k_{ij}^{23} &= \int_{\Omega_e}\left(D_{12}\frac{\partial\psi_i}{\partial x}\frac{\partial\psi_j}{\partial y} + D_{66}\frac{\partial\psi_i}{\partial y}\frac{\partial\psi_j}{\partial x}\right)dxdy \\
k_{ij}^{33} &= \int_{\Omega_e}\left(D_{66}\frac{\partial\psi_i}{\partial x}\frac{\partial\psi_j}{\partial x} + D_{22}\frac{\partial\psi_i}{\partial y}\frac{\partial\psi_j}{\partial y} + A_{44}\psi_i\psi_j\right)dxdy
\end{aligned} \tag{B-6}$$

where

$$\begin{aligned}
&D_{11} = \frac{E_1 h_t^3}{12\left(1-\nu_{12}\nu_{21}\right)};\quad D_{12} = \frac{\nu_{12}E_2 h_t^3}{12\left(1-\nu_{12}\nu_{21}\right)};\quad D_{22} = \frac{E_2 h_t^3}{12\left(1-\nu_{12}\nu_{21}\right)};\quad D_{66} = \frac{E_{12} h_t^3}{24\left(1-\nu_{12}\nu_{21}\right)} \\
&A_{55} = k_t\frac{E_{13}h_t}{2\left(1-\nu_{13}\right)};\quad A_{44} = k_t\frac{E_{23}h_t}{2\left(1-\nu_{23}\right)}
\end{aligned} \tag{B-7}$$